Dolomitization of early-post rift Lower Jurassic carbonate platforms along the Moroccan Atlantic Margin: Origin and significance

Journal of African Earth Sciences 211 (2024) 105167

Contents lists available at ScienceDirect

Journal of African Earth Sciences

journal homepage: www.elsevier.com/locate/jafrearsci

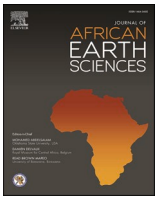

Dolomitization of early-post rift Lower Jurassic carbonate platforms along the Moroccan Atlantic Margin: Origin and significance

Nawwar Al-Sinawi [a,b,**], Cathy Hollis [b,*], Aude Duval-Arnould [b], Ardiansyah Koeshidayatullah [c], Stefan Schröder [b], Jonathan Redfern [b]

[a] Petroleum Development Oman LLC (PDO), Al Fahal Street, P.O. Box 81, PC 100, Muscat, Sultanate of Oman
[b] University of Manchester, North Africa Research Group, Oxford Road, Manchester, M13 9PL, UK
[c] Department of Geosciences, College of Petroleum Engineering and Geosciences, King Fahd University of Petroleum and Minerals, Dhahran, Saudi Arabia

ARTICLE INFO

Handling Editor: Dr Mohamed Mohamed G Abdelsalam

Keywords:
Early jurassic carbonates
Seawater dolomitization
Salt diapirism
Hydrocarbon emplacement
Morocco

ABSTRACT

Dolomitization is the most significant diagenetic process to affect Jurassic carbonate reservoirs along the Central Atlantic Margin (CAM). Despite several studies on dolomitization from different parts of CAM, the origin of these dolomites and their influence on the subsequent diagenetic evolution of Jurassic carbonate systems remains enigmatic. In addition, while dolomitization is evident at the surface and in the subsurface of the Moroccan Atlantic Margin, virtually no detailed studies have been conducted to determine the origin, mechanism, and significance of dolomitization in this basin. Therefore, the principal objective of this study is to assess the origin and occurrence of dolomite in the of Upper Sinemurian-Lower Pliensbachian carbonates of the Arich Ouzla Formation in the Essaouira-Agadir Basin by using petrography and geochemistry.

The shallow marine carbonates of the Arich Ouzla Formation have been partially dolomitized and are exposed on the salt-cored Amsittene Anticline. The dolomite is stratabound, and predominantly fabric-retentive, although in some parts it is partially replaced by non-stratabound, fabric-destructive dolomites. From petrographic observations and geochemical proxies, the fabric-preserving dolomites show dolomitization by reflux of mesohaline seawater ($\delta^{18}O_{dolomite}$ average = −3.5 ‰ VPDB, and $\delta^{13}C_{dolomite}$ average = 2.0 ‰ VPDB). In contrast, petrographic and geochemical characteristics of the fabric destructive dolomites suggest precipitation from modified seawater/formational brines convected along faults and fractures evidenced by depleted $\delta^{18}O$ isotopic values (average = −4.1 ‰ VPDB) with high fluid temperatures (average = 78 °C; range = 66–90 °C) where fluids interacted with the basal Triassic evaporites and siliciclastic sediments.

Fabric preserving dolomite has higher porosity (average = 6.0 %) than the precursor limestones (average = 0.4 %), whereas permeability in both rock types (average = 0.48 mD, and average = 0.02 mD, respectively) is low. Fabric destructive dolomite has low porosity in proximity to fracture corridors (average = 1.9 %) due to dolomite recrystallization (overdolomitization), whereas porosity increases to an average of 7.4%, away from fracture corridors. The dolomites are post-dated by calcite cement which occludes vugs, intercrystalline pores and fractures. The calcite is interpreted to be meteoric in origin, because of its non-cathodoluminescence and depleted $\delta^{18}O$ (average = −4.7 ‰ VPDB) and $\delta^{13}C$ (average = −9.3 ‰ VPDB) isotopic values with respect to Jurassic marine carbonates. The meteoric calcites co-exist with bitumen suggesting that hydrocarbon migration in the basin likely occurred at the same time, most likely during basin inversion and exposure. This work considers dolomitization to be a localised process due to salt diapirism and demonstrates that the coincidence of hydrocarbon emplacement with basin inversion results in degradation and probably leakage of hydrocarbons. This emphasises the importance of local and regional tectonics, including salt diapirism, on patterns of diagenetic overprint in sedimentary basins.

* Corresponding author.
** Corresponding author. Petroleum Development Oman LLC (PDO), Al Fahal Street, P.O. Box 81, PC 100, Muscat, Sultanate of Oman.
E-mail addresses: Nawwar.ns.sinawi@pdo.co.om (N. Al-Sinawi), Cathy.hollis@manchester.ac.uk (C. Hollis).

https://doi.org/10.1016/j.jafrearsci.2023.105167
Received 30 July 2023; Received in revised form 21 December 2023; Accepted 21 December 2023
Available online 1 January 2024

1. Introduction

Dolomitization can occur in various settings from near surface to deep burial. Dolomitizing fluids are usually seawater, often with increased salinity and/or temperature (Adams and Rhodes, 1960; Simms, 1984; Whitaker and Xiao, 2010; Al-Helal et al., 2012; Gabellone et al., 2014; Gabellone and Whitaker, 2016; Breislin et al., 2020), or formational fluids, released from deep sedimentary successions (Warren, 2000; Breislin et al., 2023) or the deep crust (e.g. Koeshidayatullah et al., 2020). Dolomite strata are associated with major carbonate petroleum reservoirs globally (Drivet and Mountjoy, 1997; Cantrell et al., 2004; Wierzbicki et al., 2006; Amel et al., 2015) often having a positive impact on reservoir quality. Dolomites are common in the Jurassic of Morocco, and are important to subsurface reservoir presence, but exact mechanisms for formation remain poorly understood. A number of studies have hypothesized various possible origins and mechanisms of dolomitization in Jurassic strata in nearby basins: (i) shallow burial from seawater at low temperatures (<50 °C) (e.g. North Pyrenean Zone & Basque-Cantabrian Basin: Bahnan et al., 2021 & Motte et al., 2021; Gibraltar: Qing et al., 2001; Eastern Morocco: Aujjar and Boulegue, 2003; Central High Atlas: Moragas et al., 2019); and (ii) deeper burial from seawater and/or formational brines at high temperatures (>50 °C), where the Mg rich brines are derived from Triassic clay minerals and evaporites (e.g. Aujjar and Boulegue, 2003; Panuke Gas Field: Wierzbicki et al., 2006; Moragas et al., 2019; Motte et al., 2021; Cruset et al., 2023). However, no detailed study on dolomitization has previously been conducted in the Western High Atlas. Jurassic dolomitized carbonates are thought to be important reservoirs along the offshore Central Atlantic Margin, but a key challenge to reduce the risk for future exploration is predicting reservoir quality in the subsurface. This study provides an analogue for understanding these offshore partially dolomitized carbonate platforms to the west of the Essaouira-Agadir Basin, particularly those which have underlying salt. The main aims of this paper are twofold: (i) to understand how basin architecture, including the role of salt halokinesis, stratal architecture and fracturing controlled the spatio-temporal distribution of dolomite on the Moroccan Atlantic Margin, and (ii) to decipher the relationship between diagenesis, facies architecture and post-rift basin tectonics. Some of the data has previously been presented in Koeshidayatullah et al. (2022), which described the dolomite – limestone reaction fronts and diagenetic boundaries. The aim of this study is to develop a holistic interpretation for the diagenetic evolution of the Arich Ouzla Formation to understand the role of basin evolution on dolomitization in the Lower Jurassic.

2. Geological setting and lithostratigraphic framework

2.1. Structural evolution

The geodynamic development of the Western High Atlas Mountain range is closely related to the Mesozoic breakup of Pangea and the opening of the Proto-Atlantic (Beauchamp, 1988). This study was conducted in the Essaouira-Agadir Basin (EAB), situated on the western coast of Morocco, southwest of the High Atlas Mountain range (Fig. 1). The EAB is bordered to the north by the Jebilet mountain range, to the east by the Massif Ancien and to the south by the Souss Basin (Fig. 1). The outcropping Mesozoic (Triassic, Jurassic and Cretaceous) succession onshore in the EAB (Fig. 1) is recognized as one of the most complete and well exposed stratigraphic successions of NW Africa (e.g. Hafid, 2000; Luber, 2017; Duval-Arnould, 2019), which reaches up to c. 7 km in thickness (Ellouz et al., 2003; Zühlke et al., 2004; Tari and Jabour, 2013). The structural evolution of the EAB can be divided into three key phases.

1) The Central Atlantic rifting phase (Fig. 2 A) formed a sag basin (Schettino and Turco, 2011), which became filled by continental siliciclastic deposits and evaporites which are the oldest sediments of Triassic age (Olsen et al., 2003; Mader and Redfern, 2011). The Triassic deposits are capped by tholeiitic basalt of the Central Atlantic Magmatic Province (Vergés et al., 2017) (Fig. 2 A). Rifting ended with the emplacement of the first oceanic crust during the Lower Jurassic (Piqué et al., 1998; Hafid, 2000) (Fig. 2 A).
2) The post-rift Pre-Atlasic phase (Fig. 2 A) led to development of a passive margin characterised by deposition of Jurassic shallow marine carbonates interbedded with marine and fluvial siliciclastic strata (Adams, 1979; Frizon de Lamotte et al., 2008; Duval-Arnould et al., 2021). This was followed by deposition of Cretaceous-aged mixed carbonate-clastic inner to outer shelf-open marine deposits composed of limestones, shales and sandstones (Frizon de Lamotte

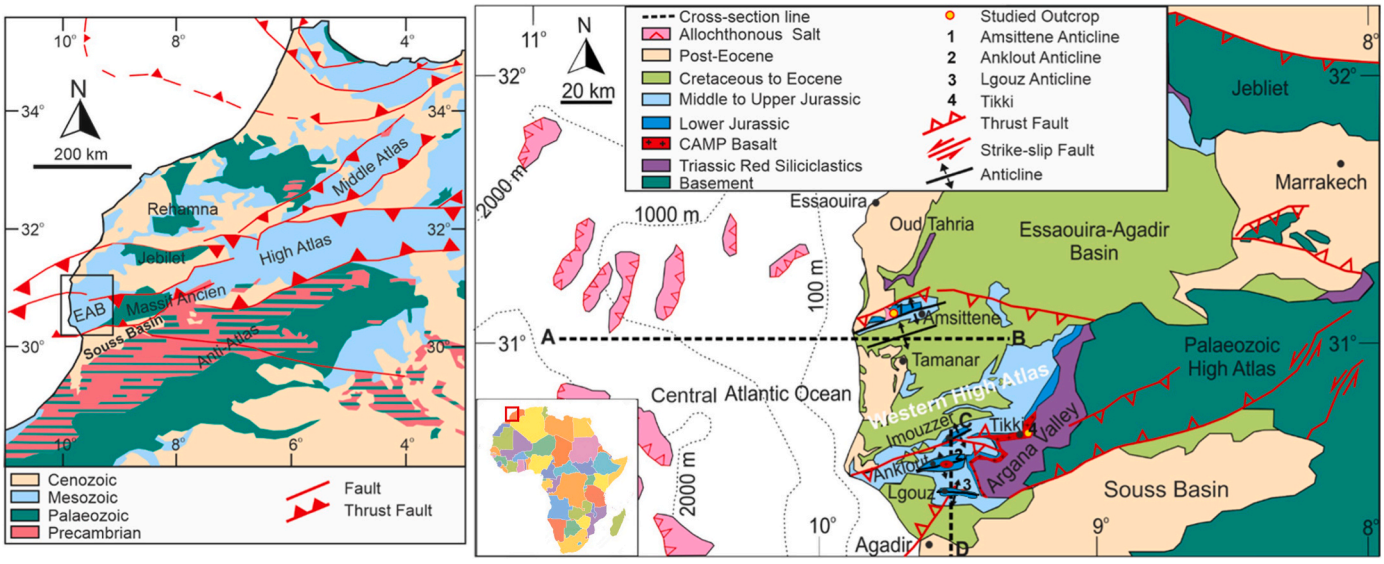

Fig. 1. Structural map (left) of northwestern Africa illustrating the main physiogeographic provinces of Morocco, the main cover of sediments and the location of the Essaouira-Agadir Basin (EAB) (modified after Hafid et al., 2006; Michard et al., 2008; Ellero et al., 2012). Geological map (right) of the EAB comprising salt-rich basin offshore and highlighting the studied outcrops in the Amsittene Anticline and Tikki as well as the outcropping structures, Central Atlantic Magmatic Province (CAMP) basalts and the location of cross-section lines (modified after Ager, 1974; Mustaphi et al., 1997; Hafid, 2000; Zühlke et al., 2004; Frizon de Lamotte et al., 2008; Tari and Jabour, 2013). The cross-section lines indicated on Fig. 1 are shown on Fig. 2 (B–C).

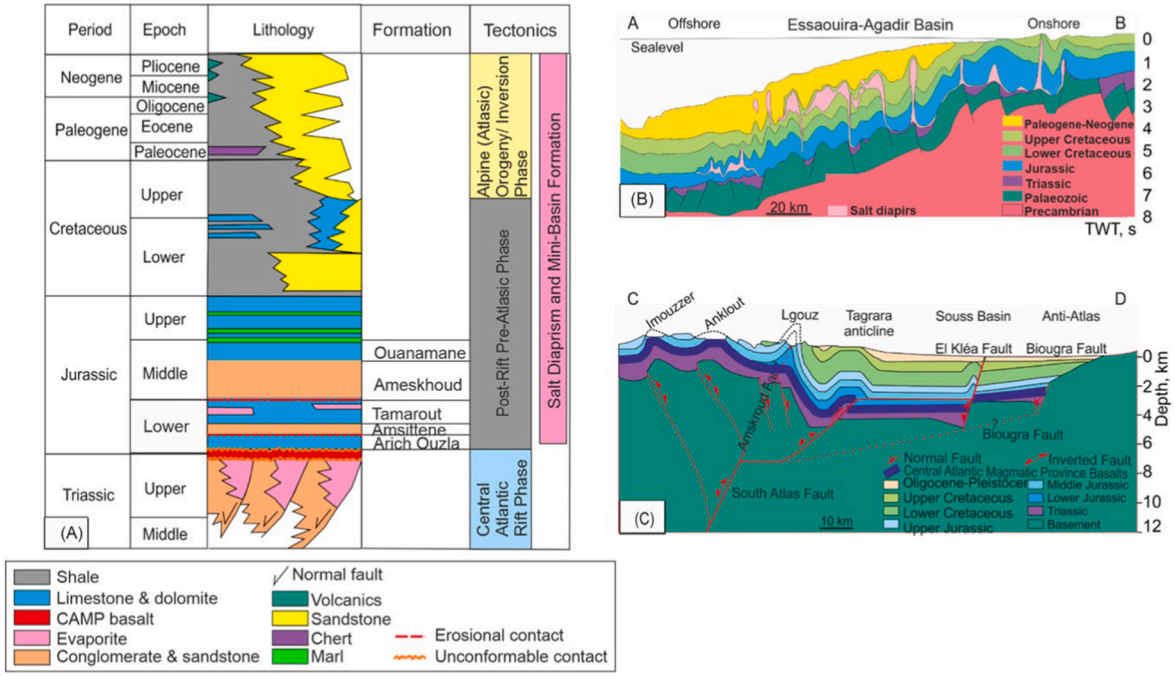

Fig. 2. (A) Chronostratigraphic column of the Essaouira-Agadir Basin and the corresponding tectonic events (modified from Zühlke et al., 2004; Frizon de Lamotte et al., 2008; Tari and Jabour, 2013; Vergés et al., 2017; Duval-Arnould, 2019). (B) Cross-section A to B showing the overall basin structure offshore and salt diapirs (modified after Tari and Jabour, 2013). (C) Cross-section C to D depicting the southern segment of the basin, affected by inverted flower structure fault system (modified after Frizon de Lamotte et al., 2008).

et al., 2008; Luber, 2017). Offshore from the Essaouira-Agadir Basin, the Triassic series are capped by 6–7.5 km thick (5–6 s TWT) Mesozoic to Cenozoic deposits that were affected by diapirism (Pichel et al., 2019; Tari and Jabour, 2013) (Fig. 2 B). Salt diapirism was coeval with Jurassic to Cretaceous sedimentation, resulting in local deformation of the strata, formation of 4–5 km thick diapirs and development of mini-basins-(Hafid et al., 2006; Tari and Jabour, 2013; Pichel et al., 2019).

3) The Alpine (Atlasic) Orogeny/Inversion phase (Fig. 2 A), due to collision of the African and European plates, from the Upper Cretaceous (Cenomanian) to the Neogene (Miocene to Pliocene) (Frizon de Lamotte et al., 2008; Vergés et al., 2017). The Atlasic Orogeny, combined with local reactivation of previous salt-related structures, led to reactivation (inversion) of the former (Triassic) rift-related (strike-slip and normal) faults in a east-northeast to west-southwest trend (Fig. 1); buckling of the Mesozoic sedimentary cover (Fig. 2B–C); development of generally east-west trending anticlines that crop out in the Essaouira-Agadir Basin and formation of thrust faults, typically with positive flower structures (Fig. 1) (e.g. Morabet et al., 1998; Hafid, 2000; Le Roy and Piqué, 2001; Zühlke et al., 2004; Hafid et al., 2006; Frizon de Lamotte et al., 2008; Ouajhain et al., 2011; Ellero et al., 2012; Tari and Jabour, 2013).

2.2. Lithostratigraphy

In the Essaouira-Agadir Basin, Triassic conglomerates, sandstones and evaporites are up to 3650 m in thickness (Frizon de Lamotte et al., 2008). These sediments filled the sag basin that was created during Triassic Central Atlantic rifting (Fig. 2 A) (Brown, 1980; Du Dresnay, 1988; Hofmann et al., 2000; Tourani et al., 2000; Piqué et al., 2002; Olsen et al., 2003; Frizon de Lamotte et al., 2008; Tourani et al., 2010; Mader and Redfern, 2011; Ellero et al., 2012). The Central Atlantic Magmatic Province (CAMP) basalt unconformably overlies, or is interbedded with, Upper Triassic to Lower Jurassic sediments (Ager, 1974; Zühlke et al., 2004; Vergés et al., 2017) (Fig. 2 A). The CAMP basalt ranges in thickness from 60 to 140 m and crops out in the Argana Valley, Tikki and the Anklout Anticline (Fig. 1). The post-rift lithostratigraphy of the Lower Jurassic in the Essaouira-Agadir Basin has been extensively described (Roch, 1930; Ambroggi, 1963; Duffaud, 1960; Adams, 1979; Adams et al., 1980; Peybernès et al., 1987; Du Dresnay, 1988; Bouaouda, 2007; Ouajhain et al., 2011; Duval-Arnould, 2019). The Arich Ouzla Formation (Upper Sinemurian to Lower Pliensbachian; Fig. 2 A), unconformably overlies Triassic siliciclastic sediments and records the onset of the earliest post-rift phase in the Essaouira-Agadir Basin (Ouajhain et al., 2011; Duval-Arnould et al., 2021). The Arich Ouzla Formation was deposited in an open marine setting on a carbonate ramp (Duffaud, 1960; Duffaud et al., 1966; Ouajhain et al., 2011; Duval-Arnould et al., 2021). The top of the Arich Ouzla Formation was eroded prior to deposition of siliciclastic sediments of the Amsittene Formation (Duval-Arnould et al., 2021) (Fig. 2 A). This formation is locally preserved onshore, to the NW of the Essaouira-Agadir Basin, in the Amsittene Anticline (Fig. 1) with a thickness of up to 84 m (Duval-Arnould et al., 2021) in outcrop. It is composed of bedded, partially dolomitized carbonates dominated by ooidal-peloidal grainstones, oncoidal floatstone and skeletal grainstones (Ouajhain et al., 2011; Duval-Arnould et al., 2021). The upper part of the formation is highly dolomitized (Duval-Arnould et al., 2021).

3. Methodology and dataset

This study was conducted during a single field season, in December 2017, during which the sedimentary section was logged and georeferenced samples were taken from the studied location (Fig. 1). Samples are representative of all depositional facies and all paragenetic phases observed in the field, including replacive dolomite and calcite as well as cements of dolomite and calcite A total of 40 standard thin sections were first stained with alizarin red S and potassium ferricyanide (Dickson, 1966) in order to qualitatively discriminate between calcite and dolomite and qualitatively assess iron content of these minerals. Glass cover slips were then applied and the sections were studied using transmitted,

polarizedlight microscopy using a Nikon Eclipse LV100NPOL microscope. All thin sections were impregnated with blue-epoxy resin to identify porosity. Cathodoluminescence (CL) examination of 6 polished, non-stained, uncovered thin sections was carried out using a Cambridge Image Technology Limited (CITL) Mk5 cold cathode stage to determine calcite and dolomite phases and origins. The CL microscope operating settings were set from 10 to 17 kV for the acceleration voltage of the electron beam and 500–600 μA for the beam current.

Mineralogy of 41 powder samples of bulk limestones, fabric preserving dolomites, fabric destructive dolomites and specifically selected phases of calcite cements collected from the logged outcrop were determined using a Bruker D8 Advance X-ray Diffractometer (XRD) at the University of Manchester. The powder samples were prepared using agate pestle and mortar (for bulk rock samples) or micro-drilled using 0.05 mm drill bit (for cement phases). Operating conditions for the XRD were: 40 kV accelerating voltage, 40 mA electron beam current, 0.02° step size with 0.2 seconds/step. The equipment tube has 0.6 exit slit and a Göbles mirror and the detector is a Lynxeye with a 0.4 mm Soller slit. The detection limit of the equipment is ~0.5% by mass. We quote the calculated percentages and errors to one decimal place. Raw XRD data were interpreted using EVA standard peak-fitting software, where raw data were normalized after background extraction to remove negative counts and peak displacement. Corrections were made using a quartz internal standard. Each peak/phase in the XRD pattern represents a mineral which was matched with the available directory. For quantitative mineralogy, Topas 4.2 software was used, which uses full pattern fitting Rietveld refinements for quantification, where the errors were calculated to be 0.01–0.1%. The stoichiometry of the dolomite ($MgCO_3$) and the degree of ordering were calculated from the XRD pattern following the equation proposed by Lumsden (1979):

$NMgCO_3 = 333.33 \times d - 911.00$ (where d = dolomite peak reflection intensity value) and ratio between 015/0110 peaks, respectively.

Carbonate-powdered bulk rock and cement samples (each sample = 0.30 mg ± 0.04 mg) from the Arich Ouzla Formation (n = 20) were analysed for their $\delta^{18}O$ and $\delta^{13}C$ isotopic ratios at Liverpool Isotope Facility for Environmental Research at the University of Liverpool, UK. Calcite powder samples were reacted with phosphoric acid under vacuum to release CO_2 at 25 °C for 30 min (*sensu* McCrea, 1950). Dolomite powder samples that were intermixed with <5% calcite were treated with ethylene diamine tetraacetic acid (EDTA) at 60 °C for 16 h under vacuum to dissolve the calcitic phase and liberate CO_2 from dolomite (Videtich, 1981). The CO_2 was then analysed for carbon and oxygen-isotopes composition on a VG SIRA 12 gas-source mass spectrometer. The precision measurement was ±0.2 ‰ for $\delta^{18}O$ and $\delta^{13}C$. All stable isotopes of carbon and oxygen values are reported in ‰ relative to the Vienna Pee Dee Belemnite (VPDB) standard.

One powdered sample each of bulk host limestone and fabric preserving dolomite were analysed for $^{87}Sr/^{86}Sr$ ratios by dissolving each 50 mg sample with 1.5 ml HNO_3 for 24 h at 50 °C to remove common carbonate minerals. For strontium separation, the methodology of Pin et al. (1994) was followed. Strontium isotope analyses were performed on a Thermo Neptune multi-collector- Inductively Coupled Plasma Mass Spectrometry (ICP-MS) at the Geochronology and Isotope Geochemistry General Research Services Centre, Faculty of Science and Technology at the University of Basque Country in Spain. For analytical correction, the procedure after Balcaen et al. (2005) was followed. The $^{87}Sr/^{86}Sr$ measured values were reported to an NBS-987 standard: 0.710220 ± 0.000001 (n = 3, 2 SD).

Three powdered samples, one of bulk host limestone & two of fabric destructive dolomite were selected for clumped isotopes analysis. Samples consisted of 8–10 mg of powder and were digested following the routine established in Murray et al. (2016) and Swart et al. (2016) to identify their Δ_{47} ratios. The samples were analysed in dual-inlet Thermo Scientific 253 and 253+ ultra-high-resolution isotope ratio mass spectrometers. Temperature data were obtained after conversion of the Δ_{47} ratios using the equation proposed by Staudigel et al. (2018), adjusted for reaction at a temperature of 90 °C, without application of acid fractionation factor. For the measured $\delta^{18}O$ isotope values of clumped isotope samples, a fractionation correction of 1.0008 was applied (after Sharma and Clayton, 1965; Land, 1980; Swart et al., 2016). The composition of the parent fluid ($\delta^{18}O_w$) for calcite samples was calculated from the calibration of Kim and O'Neil (1997). The $\delta^{18}O_w$ for higher temperature dolomite was calculated using the fractionation equation of Horita (2014) and for low-temperature dolomite samples the calibration of Matthews and Katz (1977) was used. Clumped isotope analysis was carried out at the Stable Isotope Laboratory, University of Miami.

A total of 5 powder samples, comprising bulk host limestone (1), fabric preserving dolomite (2) & calcite cement (2) were used for major ion (Ca, Mg, Na, Fe, Mn, S, Al, Sr and Si) and rare earth elements (REE) analyses. Trace elemental (major ion) analyses were conducted using a PerkinElmer Optima 5300 dual view Inductively Coupled Plasma Atomic Emission Spectroscopy (ICP-AES), whereas REE were analysed using Agilent 7700x ICP-MS. Each sample (50–100 mg) was reacted with 2 ml of 20% hydrochloric acid (HCl) overnight and 10 ml de-ionized water to ensure total dissolution of solids. The solutions were then acidified by 2% nitric acid (HNO_3) and filtered to remove particles >0.45 μm in size. The ICP-AES/MS analyses detection limits are 0.01 ppb in solution under normal operating settings. The REE concentrations of the samples were normalized to Post-Archean Australian Shales (PAAS) (Nance and Taylor, 1976) and their anomalies (Eu, Ce, Pr and Gd) were calculated following the formulas suggested by Bau and Dulski (1996).

Porosity and permeability analyses were performed on 1 inch diameter, cleaned and dried core plug samples from the Arich Ouzla Formation (n = 5) using a Digital Helium Porosimeter (DHP)-100 ResLab and Digital Gas Permeameter (DGP)-200 ResLab, respectively at University of Manchester. Details of sample preparation for porosity and permeability analyses can be found in Al-Sinawi (2022). The DHP operating conditions used a supply of 10 bars of helium gas and 6 bars of compressed air, and porosity was calculated according to Boyle's Law for total porosity values. The DGP operating settings used a supply of 6 bars of nitrogen gas and applied 10–18 bars of confining pressure. Darcy's Law was used to calculate permeability and a Klinkenberg correction was applied on all samples.

Quantitative Evaluation of Minerals by Scanning Electron microscopy (QEMSCAN) analysis of a CAMP basalt collected from an outcrop in Tikki (Fig. 1) were made using a Bruker XFlash energy dispersive X-ray spectrometer (EDS) combined with backscattered electron (BSE) intensity from a scanning electron microscope to create a mineralogy phase map. The operating settings for developing the mineralogy phase map were: 20 μm step size and 1000 counter per pixel for EDS spectra. The BSE brightness was adjusted using quartz standards and the mineralogy map was produced using QEMSCAN IExplore software, where the minerals measured spectrums were matched with an existing mineral archive known as the Species Identifican Protocol.

4. Results

4.1. Outcrop observations

The Arich Ouzla Formation (Fig. 2 A) was studied in the Amsittene Anticline (Fig. 1), which is the only outcrop of these strata in the Essaouira-Agadir Basin. The unit occurs as laterally continuous carbonate beds with a total thickness of 32.5 m (Fig. 3 A to D). The logged section is in the middle part of the formation and comprises two main lithological units (Fig. 3 C). Unit 1 (13.5 m thick) forms the lowermost to middle interval of the logged section (Fig. 3 C). It comprises well-bedded to massively bedded, grey, partially dolomitized limestone with oncoids, ooids, bivalve and gastropod shell fragments and poorly preserved undifferentiated skeletal debris (oncoidal-ooidal packstones-grainstones) which have been fractured and exhibit bed parallel stylolites (Fig. 3

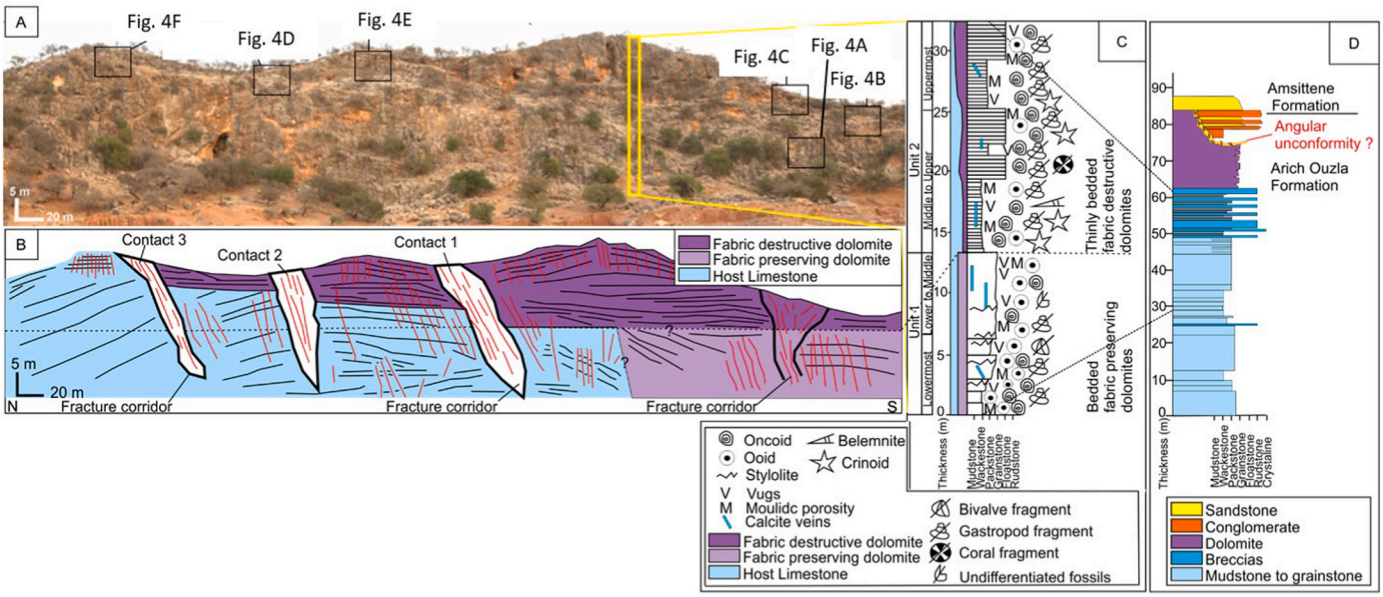

Fig. 3. (A) Panoramic overview of the Arich Ouzla Formation cropping out in the Amsittene Anticline. (B) A sketch of Fig. 3 A showing distribution of the limestones, dolomites, contacts between the limestones and the dolomites and the outcropping fractures. (C) Logged section of the Arich Ouzla Formation. (D) Sedimentary log of the Arich Ouzla Formation (modified after Duval-Arnould et al., 2021).

C). Unit 2 (19 m thick) forms the middle to uppermost part of the logged section (Fig. 3 C) and consists of well-bedded grey limestone. It contains micritised and coated grains, crinoids, coral fragments, gastropod fragments, and rare belemnite forming skeletal packstone/floatstones (Fig. 3 C).

In Unit 1, two fine-grained, fabric preserving (FP) dolomite bodies occur, which become thicker and wider up-section (Fig. 3A–C). The transition between the FP dolomite and the host limestones in Unit 1 is diffuse, with no distinct colour contrast (Fig. 3 B). The lowermost interval consists of FP dolomite which is 6.4 m thick and up to 120 m wide replacing well-bedded oncoidal-ooidal grainstones-packstones (Fig. 3 C). The lower to middle interval comprises FP dolomite that is 7.1 m thick and up to 150 m wide within a massive bed of oncoidal-ooidal grainstones (Fig. 3 C) (Fig. 4 A). The FP dolomites in Unit 1 are crosscut by bed parallel stylolites (Fig. 3 C) which are themselves crosscut by bed-inclined and bed-perpendicular calcite veins (Fig. 3 C).

In Unit 2, three medium-to coarse-crystalline, fabric destructive (FD) dolomite bodies were identified within thinly bedded, coated-grain and skeletal packstone/floatstones. The dolomite body becomes thicker and extends laterally towards the top of the unit (middle: 5.2 m thick and 152 m wide; middle to upper: 6.6 m thick and 178 m wide; uppermost: 7.2 m thick and 214 m wide) (Figs. 3 and 4 B). Although this unit has been replaced by FD dolomite, some of the large (2–4 cm in diameter) undifferentiated skeletal grains could still be seen in outcrop (Fig. 3). The contact between the FD dolomite bodies is diffuse vertically (Figs. 3 and 4C), whereas, the contact between the FD dolomite (light grey) and the host limestone (dark grey) is marked by a distinct colour contrast, with bed-perpendicular terminations bounded by three spatially distinct fracture corridors (Figs. 3 and 4D).

4.2. *Fracture characteristics*

The dolomitized part of the Arich Ouzla Formation is stratabound and relatively more fractured (8–14 fractures per meter) compared to the limestones (5–9 fractures per meter) (Fig. 3 A-C, 4 A-D). In outcrop, two main sets of fractures were identified: perpendicular (335° to 355°, n = 44) and sub-parallel (90° to 105°, n = 7) to the axis of the anticline (ENE-WSW) which are also bed-perpendicular and oblique to the bedding regardless of bedding orientation (Fig. 3 A-C and Fig. 4). Three separate fracture corridors (NNW-SSE) that range from 2 to 10 m in width and approximately 25 m in length were recorded (Fig. 3 A-B, 4 C-D). The fracture corridors consist of brecciated areas with poorly sorted, angular to sub-rounded dolomite and limestone clasts (<1 cm up to 30 cm in diameter). Calcite cements occur as white calcite pockets (<1 cm to few cm in diameter) and veins (<1 cm to few cm in diameter) that are perpendicular and oblique to the bedding (Fig. 3 C) (Fig. 4 D) and occasionally co-exist with bitumen filled vugs (<1 cm to few cm in diameter) and veins (<1 cm to few cm in diameter) (Fig. 4E–F). Downward tapering fissures from the uppermost layer, pass into irregularly shaped vertical pipes (<1 m in width) within the fracture corridors and extend to 5 m in depth and up to 10 m in width. They host poorly sorted, angular to sub-rounded limestone and dolomite clasts (<1 cm–30 cm in diameter) supported by red, very fine grained occasionally laminated sandy-silty carbonate mudstone (Fig. 4 F).

4.3. *Arich Ouzla Formation limestone geochemistry*

The Arich Ouzla Formation Unit 1 limestones were not analysed geochemically as no host limestone physical rock samples were collected from this unit. Unit 2 limestones comprise minor quartz (4.7%), dolomite (3.0%) and albite (0.6%) (Table 1). Unit 2 limestones have an average $\delta^{18}O = -3.8$ ‰ VPDB (−4.1 to −3.5 ‰ VPDB) and $\delta^{13}C = 1.2$ ‰ VPDB (0.5–1.8 ‰ VPDB) (Fig. 5A, Table 2). The $^{87}Sr/^{86}Sr$ ratio measured on a limestone sample in Unit 2 was 0.7083 (Fig. 5B). The clumped isotope temperature, calculated from $\Delta_{47} = 0.49$ of Arich Ouzla Formation Unit 2 limestone was 69 °C (Table 2). Unit 2 limestone has high concentrations of Mg (6190 ppm), Fe (2450 ppm), S (6100 ppm), Si (13920 ppm), Na (1150 ppm) and Al (1260 ppm), and relatively low concentrations of Mn (152 ppm) and Sr (196 ppm) (Table 1). The sum of REE and REE + Y concentrations for a limestone sample from Unit 2 is 25.2 ppm and 30.3 ppm, respectively (Table Supplementary Material). Its PAAS-normalized (REE + Y) is fairly flat (Fig. 6A) and plots within the 'no Ce anomaly' quartile using the linear method (Fig. 6B) and has PAAS normalized ratios of Eu = 1.22, Ce = 0.99, Pr = 1.00 and Gd = 1.08. Unit 2 limestone has ratios of Y/Ho = 32.6, La/Yb = 13.3 and La/Sm = 4.49 (Table Supplementary Material).

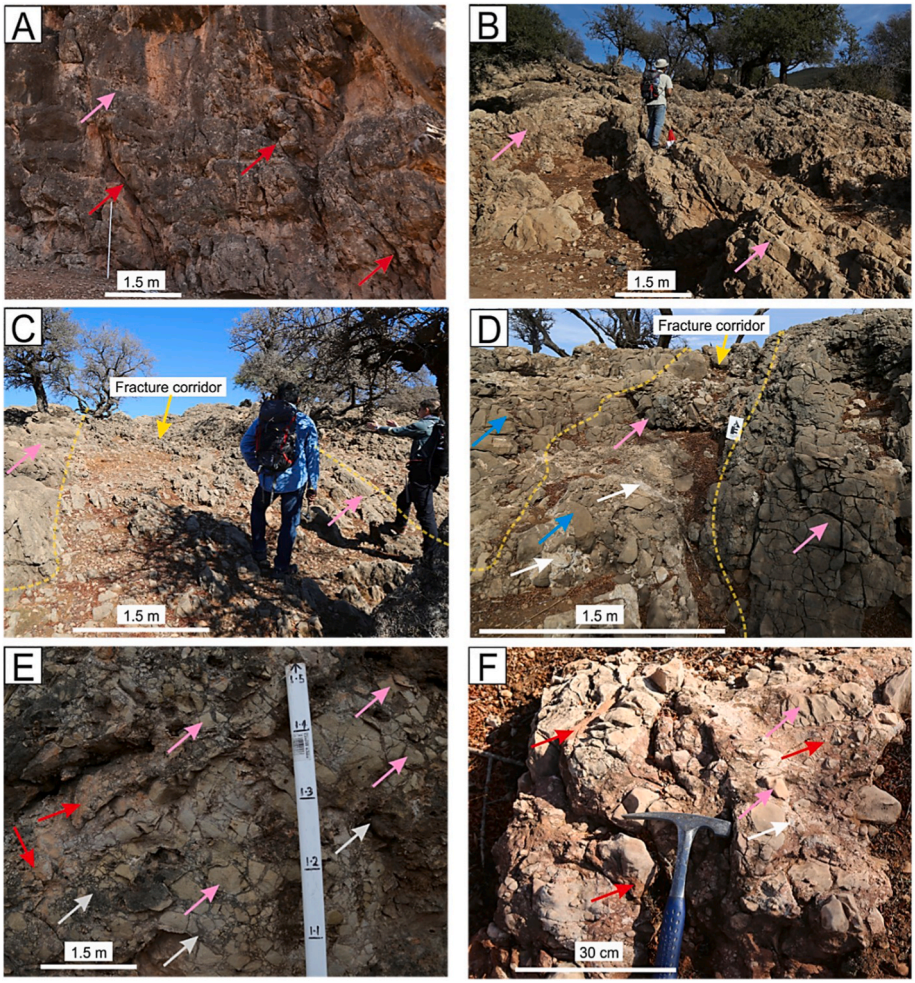

Fig. 4. Photographs of the Arich Ouzla Formation outcropping in the Amsittene Anticline, NW Essaouira-Agadir Basin. (A) NNW-SSE fractures (red arrows) observed in the fabric preserving (FP) dolomite of Unit 1 (pink arrow). (B) Thinly bedded fabric desctructive (FD) dolomite of Unit 2 (pink arrows). (C) A fracture corridor (yellow dashed line) within Unit 2, thinly bedded FD dolomite (pink arrows). (D) Unit 2 moderately fractured limestone (blue arrow) and highly fractured FD dolomite (pink arrow) bounded by a fracture corridor (yellow dashed line) where clasts of limestones (blue arrow) and dolomite (pink arrow) as well as calcite cement (white arrows) were noted. (E) Deformed FD dolomite clasts (pink arrows) from Unit 2, crosscut by a network of black cemented fractures (white arrows) and pockets filled by red sandy carbonate mudstones (red arrows). (F) A fracture corridor showing dolomite (pink arrows) brecciated by white calcite cement (white arrow) and fissures (fractures and pockets) filled by red sandy mudstone (red arrows). Locations of Fig. 4 A to F are indicated in Fig. 3.

4.4. Fabric preserving dolomite

Petrographically, 45% visual determinationof the Arich Ouzla Formation dolomite is FP dolomite. It is characterised by very fine to medium planar-e to planar-s (*sensu* Sibley and Gregg, 1987) (Fig. 7A–B). Dolomite partially nucleates on, or completely replaces, ooids and oncoids at the base of Unit 1 (Fig. 7A), with pervasive dolomitization toward the top of this unit (Fig. 7B). FP dolomite also partially replaces the micrite matrix of the coated grains and skeletal packstone/floatstone in Unit 2 (Fig. 7E). FP dolomite shows unit to undulose extinction under crossed polarized light with inclusion density (locally showing cloudy cored dolomite crystals) (Fig. 7 C). Under CL, it is characterised by dull to very dark red CL response (Fig. 7C–D).

The average stoichiometry of the FP dolomite is 41 mol % (range = 33–48 mol %) $MgCO_3$ (Table 2) and well-ordered based on the strength of the 015 peak relative to the 110 peak. It has an average $\delta^{18}O_{dolomite}$ = −3.5 ‰ VPDB (range = −4.1 to −2.8 ‰ VPDB) and $\delta^{13}C_{dolomite}$ = 2.0 ‰ VPDB (range = 1.9–2.1 ‰ VPDB) (Fig. 5A; Table 2) with a $^{87}Sr/^{86}Sr$ ratio of 0.7089 (Fig. 5B). Concentrations of Mn average 682 ppm (range = 548–815 ppm), Na concentrations average 249 ppm (range = 219–279 ppm), Fe concentrations average 2490 ppm (range = 2080–2910 ppm) and S concentrations average 3040 ppm (range = 2770–3300 ppm) (Table 1). Concentrations of Al, Sr and Si are relatively low (Table 1). The average sum of REE concentrations for FP dolomite is 7.14 ppm (range = 6.42 ppm–7.86 ppm; Table Supplementary Material). The total REE + Y concentrations for FP dolomite has an average of 9.91 ppm (range = 9.15–10.7 ppm; Table Supplementary Material). The PAAS-normalized (REE + Y) profile shows negative Ce and positive Y anomalies (Fig. 6 A), with the corrected data (after Bau and Dulski, 1996) showing a positive La and no Ce anomaly (Fig. 6 B). The PAAS-normalized Y/Ho ratios average 34.4 (range = 33.9 to 35.0; Table Supplementary Material).

4.5. Fabric destructive dolomite

Microscopically, the FD dolomite is recognized by planar-s and nonplanar anhedral (Sibley and Gregg, 1987) dolomite crystals (Fig. 7F) that range from 60 to 400 μm in diameter and show undulose to sweeping extinction under crossed polarized light. Visual petrographic estimation indicates that fabric-destructive dolomite makes up approximately 50% of the Arich Ouzla Formation dolomite volume. It can occur as clear crystals or with cloudy cores and clear rims under plain polarized light (Fig. 7F–G). Fabric destructive dolomite is characterised by very dark red CL (Fig. 7H). Although FD dolomite destroyed the host

Table 1
Mineralogical composition (%) based on XRD analysis performed on six samples (bulk limestone sample from Unit 2, n = 1; bulk FP dolomite samples from Unit 1, n = 2; specifically selected and microdrilled calcite cement samples, n = 2; bulk FD dolomite sample from Unit 2, n = 1) from the Arich Ouzla Formation in the Amsittene Anticline, and major trace elemental composition (ppm) of the Arich Ouzla Formation performed on five samples (bulk limestone sample from Unit 2, n = 1; bulk FP dolomite samples from Unit 1, n = 2; specifically selected and microdrilled calcite cement samples, n = 2 (analysed by ICP-AES).

Phase/Composition	Quartz (%)	Calcite (%)	Dolomite (%)	Albite (%)	Ca (ppm)	Mg (ppm)	Na (ppm)	Fe (ppm)	Mn (ppm)	S (ppm)	Al (ppm)	Sr (ppm)	Si (ppm)
Limestone; n=1	4.7	91.8	3.0	0.6	305600	6190	1150	2450	152	6100	1260	196	13920
FP dolomite; n=2	0.4–0.8	0.4–1.7	97.4–99.1	0.1–0.3	140900-162500	64240-70600	219–279	2080–2910	548–815	2770–3300	283–321	25.7–29.9	69–142
Calcite Cement; n=2	0.5–1.0	97.0–97.5	1.8–2.1	0.0–0.1	218900-246400	5170–7980	40.4–93.7	238–349	39.4–19550	4190–4730	482–907	22.5–40.4	97.9–161
FD dolomite; n=1	2.2	0.6	97.1	0.06	–	–	–	–	–	–	–	–	–

limestone texture in Unit 2 (Fig. 7E–H), ghosts of the original texture can still be observed microscopically. The average stoichiometry of FD dolomite is 50 mol % (range = 47–52 mol %) $MgCO_3$ (Table 2) and well ordered based on the strength of the 015 peak relative to the 110 peak. It has an average value of $\delta^{18}O_{dolomite} = -4.1$ ‰ VPDB (range = −4.9 to −3.5 ‰ VPDB) and $\delta\ ^{13}C_{dolomite} = 0.9$ ‰ VPDB (range = −0.8 to 1.8 ‰ VPDB) (Fig. 5A, Table 2). The fluid temperature was calculated from its $\Delta_{47} = 0.50$ to 0.46 as 66–90 °C (Table 2). No samples of this dolomite phase underwent trace elements analysis.

4.6. Dolomite cement

Visual petrographic determination estimates that dolomite cement in the Arich Ouzla Formation makes up an estimated <5 % of the rock volume. Microscopically, dolomite cement is characterised by very fine to medium (<10 μm to <200 μm) planar-s dolomite crystals filling mouldic porosity (Fig. 7A) or as clear dolomite cement rim/overgrowth crystals, under plain polarized light, that fill intercrystalline porosity in FP (Fig. 7C) and FD dolomite (Fig. 7F and H). It shows undulose to sweeping extinction under crossed polarized light. Under CL, the planar-s dolomite cement has dull red CL response (Fig. 7D) and the cement overgrowth rim around the FD dolomites has a bright orange CL response (Fig. 7H).

4.7. Calcite cement

Calcite cement in outcrop was found in fractures that crosscut the dolomitized Arich Ouzla Formation and in vugs, intercrystalline and mouldic porosity (Fig. 3 C, 4 D-F). The calcite cement is white (Fig. 4 D), black (Fig. 4 E) and red (Fig. 4 F) in colour. Petrographically, it comprises granular crystals that reach up to 400 μm in diameter (Fig. 7 B and G) and are pink in colour under plain polarized light (stained with Alizarin Red S; Dickson, 1966). Where the calcite cement is black in outcrop (Fig. 4 E), black bitumen secondary inclusions, which are 100's μm in size, are observed within calcite crystals which partially fill vugs, fractures and intercrystalline porosity. No other hydrocarbon fluid phases were noted. The calcite cemented fractures in outcrop co-exist with quartz grains. Calcite cement shows unit extinction under crossed polarized light and is light to dark grey under reflected light, non-fluorescent under ultra-violet light and non-CL (Fig. 7 H).

The XRD analysis of the cements indicates a composition dominated by calcite (97.0–97.5 %) with minor dolomite (1.8–2.1 %), quartz (0.5–1.0 %) and albite (0.0–0.1%) (Table 1). Calcite cement has average values of $\delta^{18}O = -4.7$ ‰ VPDB (range = −5.2 to −4.2 ‰ VPDB) and $\delta\ ^{13}C = -9.3$ ‰ VPDB (range = −10.1 to −8.6 % VPDB) (Fig. 5 A, Table 2). The calcite cement has high concentrations of Mg (average = 6570 ppm, range = 5170–7980 ppm) and S (average = 4460 ppm, range = 4190–4730 ppm) and variable Mn (average = 9790 ppm, range = 39.4–19550 ppm) (Table 1). Calcite cement has relatively low concentrations of Fe, Al, Si and Sr (Table 1). The average sum of REE concentrations for Arich Ouzla Formation calcite cement is 4.63 ppm (range = 1.12–8.13 ppm; Table Supplementary Material). The total REE + Y average is 5.73 ppm (range = 1.46–10.0 ppm; Table Supplementary Material). The PAAS-normalized (REE + Y) patterns for Unit 2 black calcite cement show a positive Ce and Y anomalies and the white calcite cement have a negative Ce and positive Y anomalies (Fig. 6 A). The PAAS-normalized anomalies of Pr and Ce of the white calcite cement plots within the positive La anomaly and no Ce anomaly quartile using the linear method (after Bau and Dulski, 1996) (Fig. 6 B). The PAAS-normalized REE anomalies are: Eu/Eu* average = 2.28 (range = 1.22 to 3.34), Ce/Ce* average = 3.04 (range = 0.87 to 5.20), Pr/Pr* average = 0.67 (range = 0.34 to 1.01) and Gd/Gd* average = 1.16 (range = 1.05 to 1.26) (after Bau and Dulski, 1996). The calcite cement Y/Ho ratio averages as 33.7 (range = 27.5 to 39.9) (Table Supplementary Material).

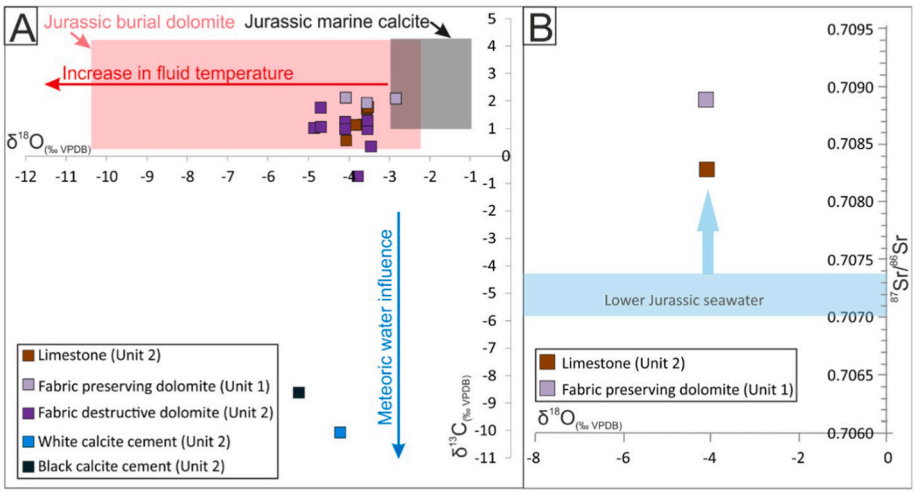

Fig. 5. Arich Ouzla Formation $\delta^{13}C$, $\delta^{18}O$ and $^{87}Sr/^{86}Sr$ isotopes data. (A) A cross-plot of $\delta^{13}C$ against $\delta^{18}O$ of Unit 2 limestones, FP dolomites, FD dolomites and calcite cements, shown relative to fields plotted from Lower Jurassic marine calcite (Veizer et al., 1999; Veizer and Prokoph, 2015) and Jurassic burial dolomite (Wierzbicki et al., 2006) plotted in VPDB. Number of samples = 20 (limestone = 6, FP dolomite = 3, FD dolomite = 9, white calcite cement = 1, black calcite cement = 1). (B) A cross-plot of $^{87}Sr/^{86}Sr$ against $\delta^{18}O$ of Unit 2 limestone and FP dolomite, shown relative to the range of $^{87}Sr/^{86}Sr$ values for Lower Jurassic seawater (Qing et al., 2001), with illustration of apparent trend. Number of samples = 2 (limestone = 1 and FD dolomite = 1).

Table 2
Limestone (number of samples = 6), FP dolomite (number of samples = 3), FD dolomite (number of samples = 9) and calcite cement (number of samples = 2) mineralogical properties and isotopic analysis from the Arich Ouzla Formation.

Phase	Dolomite Stoichiometry (mol % $MgCO_3$)	$\delta^{18}O$ (‰ VPDB)	$\delta^{13}C$ (‰ VPDB)	Δ_{47}-RF (CDES @ 90 °C)	$T\Delta_{47}$ (°C)	$^{18}O_{water}$ (‰ SMOW)
Arich Ouzla Formation Host Limestone						
Maximum		−3.5	1.8			
Minimum		−4.1	0.5			
Mean		−3.8	1.2	0.49 ± 0.016	69 ± 8.5	6.5 ± 1.2
Standard Deviation		0.3	0.5			
Arich Ouzla Formation FP Dolomite						
Maximum	48.3	−2.8	2.1			
Minimum	33	−4.1	1.9			
Mean	40.7	−3.5	2			−1.7 to 0.3 (assumed temperature @ 35–45 °C)
Standard Deviation		0.6	0.1			
Arich Ouzla Formation FD Dolomite						
Maximum	51.7	−3.5	1.8	0.50 ± 0.008	90 ± 1.4	7.5 ± 0.28
Minimum	47.3	−4.9	−0.8	0.46 ± 0.002	66 ± 3.9	3.1 ± 0.71
Mean	49.5	−4.1	0.9	0.48 ± 0.005	78 ± 2.7	5.3 ± 0.50
Standard Deviation		0.6	0.7			
Arich Ouzla Formation Calcite Cement						
Maximum		−4.2	−8.6			
Minimum		−5.2	−10.1			
Mean						−4.3 to −2.8 (assumed temperature @ 35–45 °C)

4.8. Porosity and permeability

No porosity and permeability analyses were performed on Unit 1 of the Arich Ouzla Formation limestones as no host limestones rock samples were collected from this unit. The limestones in Unit 2 exhibit low (average = 0.4%; range = 0.2–0.5%, n = 2) porosity (mouldic) and relatively very low permeability (average = 0.02 mD; range = 0.02–0.02 mD) . The FP dolomites are dominated by vugs, molds of ooids and intercrystalline porosity (average = 6.0 %; range = 0.9–11.0 %) (Fig. 7 B), and the volume of porosity increases towards the top of Unit 1 (Fig. 3 C). However, the permeability of the FP dolomite in Unit 1 is low (average = 0.48 mD; range = 0.03 to 0.92 mD). Overall, porosity is lower in FD dolomite than in the FP dolomite and decreases up-section (from average = 7.8 % to average = 2.9 %). Fabric-destructive dolomite is characterised by intercrystalline and mouldic pore-spaces (Fig. 7 F). The dolomite has lower porosity in proximity to the fracture zone, with an average of 1.9% near the fracture corridors and average 7.4% at 40 m distance from the fracture corridor.

4.9. The Central Atlantic Magmatic Province (CAMP) basalt

A basalt sample was collected from the outcrop at Tikki (Fig. 1), in the southeast of the Essaouira-Agadir Basin to determine the mineralogy and confirm the presence of Mg-rich minerals. The basalt is highly fractured and is crosscut by quartz veins (Fig. 8 A). QEMSCAN analysis shows that the CAMP basalt is composed mainly of feldspar (38.9 %), pyroxene (21.0 %), olivine (7.2 %), chlorite (10.6 %) and quartz (7.9 %) (Fig. 8 B).

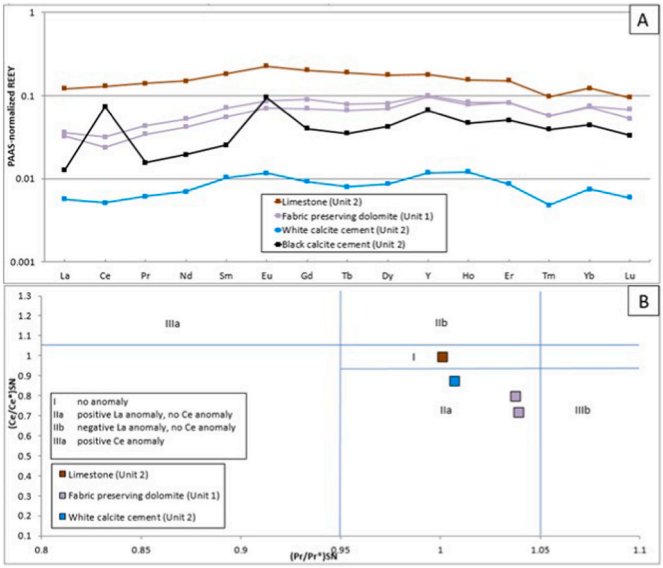

Fig. 6. REE data of the Arich Ouzla Formation limestone, FP dolomite and calcite cements, normalized to PAAS. (A) REE + Y patterns (number of samples = 5). (B) Calculated anomalies of Pr and Ce using the linear method (Bau and Dulski, 1996) (number of samples = 4).

5. Discussion

5.1. Paragenesis

In the Arich Ouzla Formation, the micrite matrix, micrite envelopes, oncoids, ooids and skeletal allochems (Fig. 7 A) within the limestone were replaced by very fine to medium crystalline planar-e and planar-s fabric-preserving (FP) dolomite forming the first phase of dolomitization (Fig. 7 B–C, 9 B) where all other diagenetic phases cross-cut and postdate this phase (Figs. 9 and 10). Bed-parallel (horizontal) stylolites crosscut the FP dolomite (Fig. 3 C 9 B) and indicate that FP dolomite formed before significant burial (<1 km; Dunnington, 1967; Alsharhan and Sadd, 2000; Machel, 2004) (Fig. 10). The finely crystalline, FP dolomite crystals (Fig. 7 B and C) are partially replaced and/or overprinted by coarser planar-s and nonplanar anhedral FD dolomite crystals (Fig. 7 F, 9 C, 10) suggesting recrystallization of the FP dolomites. Dolomite cement nucleates on cloudy, FD dolomite crystals (Fig. 7 F, 9 D) and partially occludes intercrystalline porosity (Fig. 10) and mouldic porosity and so postdates dolomitization of the limestone (Fig. 7 A, 9 D, 10). White calcite cement partially occludes fractures (Fig. 4 D) that crosscut all the dolomitized beds and dolomite cement (Fig. 7 A and G) and partially fills intercrystalline porosity. The calcite cement is locally associated with black secondary inclusions of bitumen (Fig. 4 E, 9 E); bitumen was also found between the calcite crystals filling vugs and fractures, giving it a black pigmentation, which suggests that emplacement of hydrocarbon was coincident or immediately after calcite cementation. The black calcite cemented fractures are crosscut by pockets filled by red sandy carbonate mudstones/red calcite cement (Fig. 4 E), which also fills fractures (Fig. 4 F, 9 F) and occludes remnant porosity. This is the last diagenetic phase (Fig. 10) in the Arich Ouzla Formation in the Amsittene Anticline.

5.2. Origin of FP dolomite

The stratabound distribution of dolomite and cross-cutting of dolomitized beds by stylolites indicates that FP dolomite was precipitated in the earliest stages of burial. The very fine to medium crystallinity, planar crystal textures (Fig. 4 A, B and C) and poor stoichiometry (Table 2) of FP dolomites are consistent with a rapid rate of dolomitization and high reactive surface area of the fine carbonate mud, whereas corals,

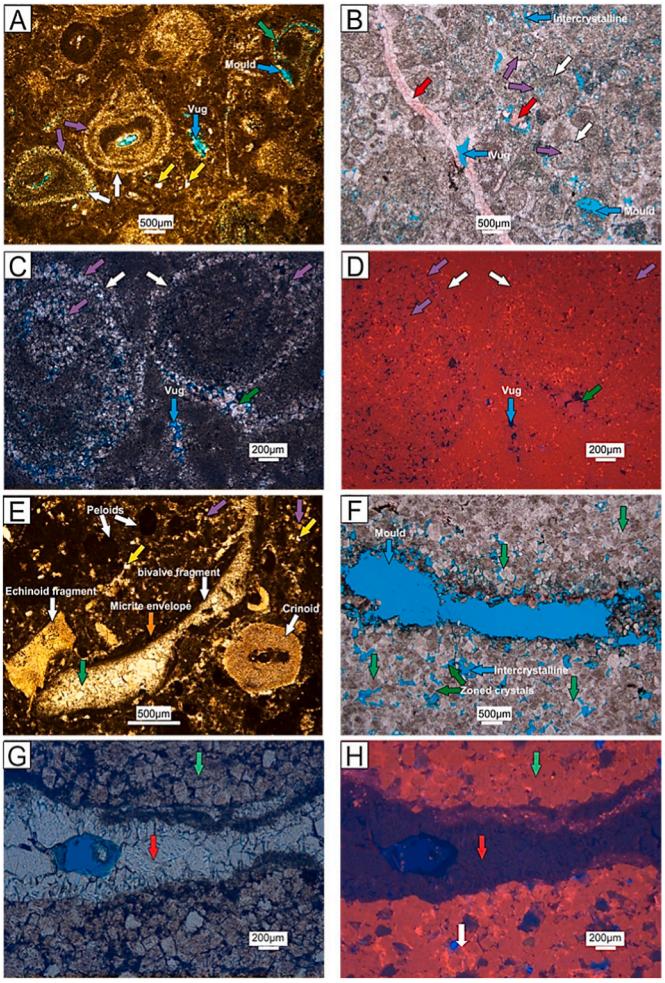

Fig. 7. Photomicrographs of the Arich Ouzla Formation. (A) Partial replacement of oncoids (white arrows) in Unit 1 by Fabric preserving (FP) dolomite (purple arrows) under plain polarized light. Mouldic porosity is illustrated by blue arrows and is partially occluded by dolomite cement (green arrow). Quartz grains are indicated with yellow arrows. (B) Partial replacement of ooids and oncoids (white arrows) within the grainstones of Unit 1 by FP dolomite (purple arrows), crosscut by calcite cement (red arrow) filling fracture under plain polarized light. Vugs, intercrystalline and mouldic porosity are illustrated with blue arrows. Calcite cement (red arrow) also found filling intercrystalline porosity. (C) Oncoids (white arrows) in Unit 1 limestones partially replaced by FP dolomite (purple arrows). Vuggy porosity is illustrated with a blue arrow, where the porosity is partially occluded by dolomite cement (green arrow). (D) Same view as (C) showing dull red CL response of the FP dolomite (purple arrows) and the dolomite cement (green arrow) under CL. (E) Partial replacement of a skeletal floatstone of Unit 2 by FP dolomite (purple arrows) and FD dolomite (green arrow) replacing a bivalve fragment under plain polarized light. The bivalve fragment is coated by micrite (orange arrow). Quartz (yellow arrows), peloids, echinoid fragment and crinoid were also noted. (F) FD dolomite (green arrows) with zoned crystals showing cloudy cores and clear rims of Unit 2, also showing mouldic and intercrystalline porosity (blue arrows) under plain polarized light. (G) FD dolomite (green arrow) of Unit 2 crosscut by a calcite cemented fracture (red arrow) under plain polarized light. (H) Same view as (G) showing dark red dull CL FD dolomite (green arrow), non-CL calcite cement (red arrow) and orange bright CL of dolomite cement overgrowth.

gastropods, echinoids and crinoids skeletal allochems were more resistant to dolomitization (Fig. 7 E) (e.g. Braithwaite and Heath, 1996; Gabellone and Whitaker, 2016). Repeated flux of dolomitizing brine would eventually lead to dolomitization of low permeability sediment, particularly since the fine-grained carbonate mud supported facies would have a high reactive surface area (Gabellone and Whitaker,

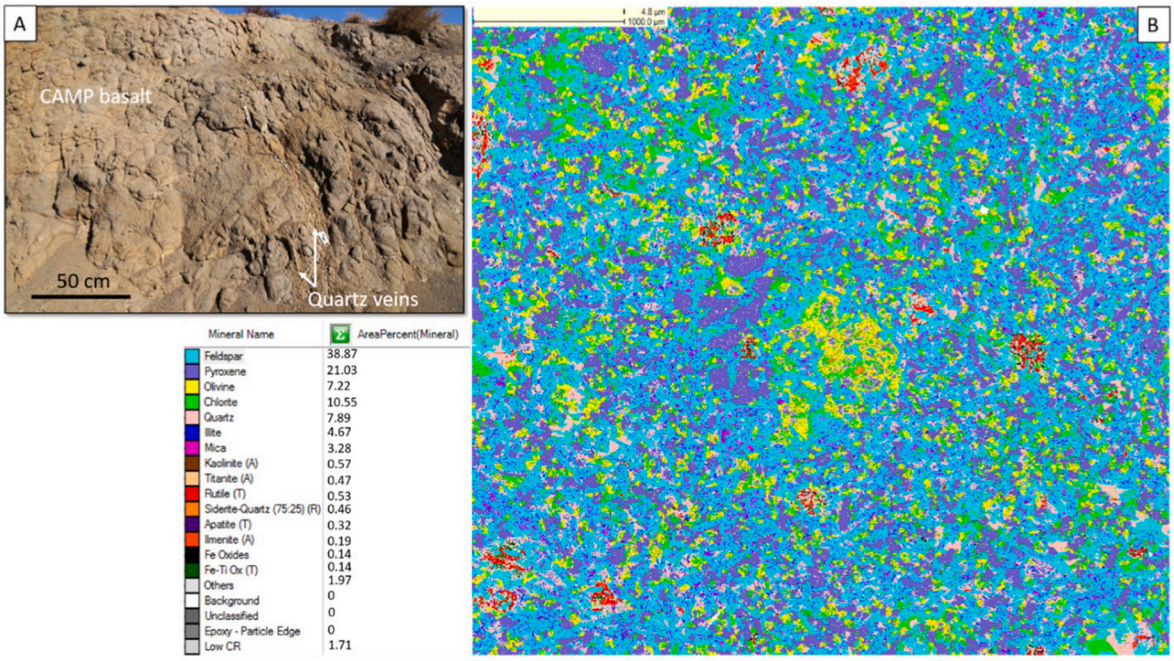

Fig. 8. (A) Field photograph showing the CAMP basalt being crosscut by quartz veins in the locality of Tikki. (B) QEMSCAN performed on the basalt sample collected from the locality of Tikki. QEMSCAN image scale bar = 1000 μm. The locality of Tikki is shown on Fig. 1.

2016).

The $\delta^{13}C$ (average = 2 ‰ VPDB; range = 1.9–2.1 ‰ VPDB) and $\delta^{18}O$ (average = 3.5 ‰ VPDB; −4.1 to −2.8 ‰ VPDB) isotopic values for the FP dolomite (Fig. 5 A) are comparable to other Lower Jurassic marine carbonates (e.g. Veizer et al., 1999; Qing et al., 2001; Veizer and Prokoph, 2015) and to the $\delta^{13}C$ and $\delta^{18}O$ isotopic values obtained from early formed dolomites encountered in the neighbouring basins, in Gibraltar (Qing et al., 2001) and in the Central High Atlas (Moragas et al., 2019). Moragas et al. (2019) noted oxygen isotope depletion of the early formed dolomites in the Central High Atlas, and proposed they could be related to elevated heat flow associated with Atlantic rifting and volcanism. Comparable $\delta^{13}C$ isotopic signatures and slightly depleted $\delta^{18}O$ isotopic values to that of Lower Jurassic marine carbonates have also been reported by Auajjar and Boulègue (2003) in Lower Jurassic dolomites of the Tazekka district, Eastern Morocco. Volcanism had stopped by the Lower Jurassic in the Essaouira-Agadir Basin (Marzoli et al., 2004; Nomade et al., 2007; Whiteside et al., 2007), the depleted $\delta^{18}O$ isotopic values (Table 2, Fig. 5 A) could be explained by an elevated seawater temperature and an elevated basal heat flux from the underlying salt (Koeshidayatullah et al., 2022), rather than diagenetic alteration during shallow burial by meteoric water circulation or alteration by dilute, lower temperature fluids (e.g. Cruset et al., 2021).

Overall, the petrographic and stable isotopic data suggests FP dolomites formed from seawater. The PAAS-normalized REE profile shows negative Ce and positive Y anomalies (Fig. 6 A) that are typical for seawater (e.g. Banner et al., 1988; Bau and Dulski, 1996; Tostevin et al., 2016), although the cross plot of normalized Ce and Pr anomalies (Fig. 6 B) (after Bau and Dulski, 1996) indicates that the FP dolomite has a positive La anomaly but no Ce anomaly, suggesting precipitation in a slightly reduced setting (e.g. Al-Aasm et al., 2021; Lécuyer et al., 2004; Tostevin et al., 2016). The dull red CL response (Fig. 7 D) and high concentration of Fe (average = 2490 ppm) (Table 1) in FP dolomite also suggests dolomitization took place in a reduced setting (e.g. Banner and Hanson, 1990; Machel and Burton, 1991; Machel, 2004; Railsback and Hood, 2001; Boggs, 2009; Hiatt and Pufahl, 2014).

The $^{87}Sr/^{86}Sr$ ratio of the FP dolomite (0.7083) is higher than Jurassic seawater (Prokoph et al., 2008), but could be explained if fluids migrated through and reacted with the underlying Triassic sandstones (Fig. 5 B, 11). Similar interpretations have been made in other basins where dolomitized strata are underlain by highly permeable sandstones (e.g., McLennan et al., 1990; Hollis et al., 2017; Newport et al., 2017; Özyurt et al., 2019; Newport et al., 2020). The variable Al (average = 302 ppm) (Table 1) concentrations, low ΣREE and ΣREE + Y concentrations (averages = 7.14 ppm and 9.91 ppm) (Table supplementary data) of FP dolomite are also consistent with seawater interaction with siliciclastic sediments (e.g. Kahle, 1965; Abanda and Hannigan, 2006; Carmichael et al., 2008), as is the Y/Ho ratio (average = 34.4; Table supplementary data) (Y/Ho ratio = 33–40, Tostevin et al., 2016).

5.3. Origin of FD dolomite

The FD dolomite replaces FP dolomite and is characterised by planars and nonplanar petrographic textures (Fig. 7 F and G), dull CL response, a stoichiometric composition (average = 49.5 mol% $MgCO_3$; range = 47.3–51.7 mol% $MgCO_3$) (Table 2), and relatively high crystallization temperatures (average = 78 °C; range = 66–90 °C) (Table 2) from isotopically enriched $\delta^{18}O_{water}$ (average = 5.3 ‰ SMOW; range = 3.1–7.5 ‰ SMOW) relative to that reported for the FP dolomite (Table 2). This suggests progressive recrystallization of the early-formed, FP non-stoichiometric dolomite (e.g. Olanipekun and Azmy, 2017). The variation in crystal size of the FD dolomite (60–400 μm in diameter) suggests that the substrate was polymodal (e.g., Sibley and Gregg, 1987; Braithwaite and Heath, 1996), whilst the uniform dull CL response (Fig. 7 H) implies a single event under burial conditions, allowing incorporation of Fe^{2+} in the crystal (Hiatt and Pufahl, 2014). The enriched $\delta^{18}O_{water}$ value could indicate fluid – rock reaction, perhaps with the underlying Triassic salts or siliciclastic sediments (e.g. Cruset et al., 2021; Cathelineau et al., 2021). A possible source of Mg for dolomitization could be penecontemporaneous or relict seawater, convected through faults and fractures, which may have interacted with siliciclastic sediments, and/or CAMP Basalts, by leaching Mg from olivine, or mixing with formational brines with the Triassic clay minerals and possibly CAMP basalts (olivine & pyroxene) (Fig. 11).

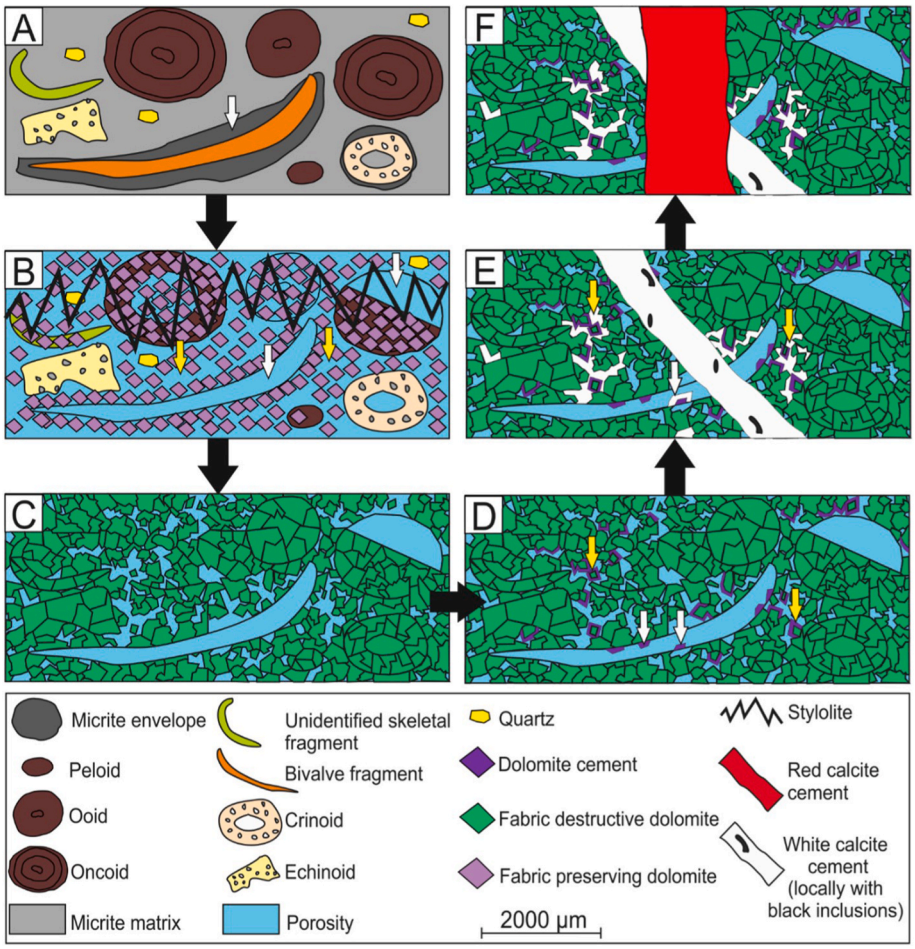

Fig. 9. A cartoon showing the paragenesis of the Arich Ouzla Formation in the locality of the Amsittene Anticline, Essaouira-Agadir Basin. (A) Micrite envelope around a bivalve shell (white arrow). (B) Replacement of the host limestone by FP dolomite which is crosscut by a stylolite. (C) Replacement by FD dolomite (green) where the original limestone fabric becomes challenging to distinguish. Reduction of the pore space (blue) relative to (B) becomes noticeable. (D) Dolomite cement partially fills intercrystalline porosity (yellow arrows) and mouldic porosity (white arrows) in FD dolomite (green). (E) White calcite cement filling intercrystalline porosity (yellow arrows), mouldic porosity (white arrow) and a fracture crosscutting the dolomites. (F) Red calcite cement crosscuts the white calcite cement.

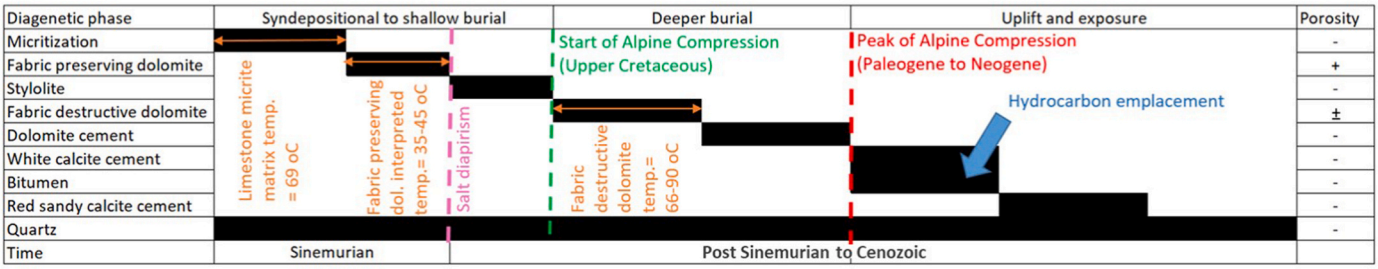

Fig. 10. Paragenetic sequence showing the relative timing of the Arich Ouzla Formation diagenetic phases associated to diagenetic realms, related to major tectonic event and the porosity enhancing (+), porosity destructive (−), porosity enhancing/destructive (±) phases.

5.4. Dolomitization model

It has been proposed that the formation of FP dolomite of the Arich Ouzla Formation took place from seawater based on the stratabound distribution of dolomite, its paragenetically early timing and geochemical data. Seawater can reflux from meso-or hypersaline brine pools on the platform top in peritidal settings leading to dolomitization of platform strata (Adams and Rhodes, 1960; Simms, 1984; Qing et al., 2001; Melim and Scholle, 2002; Jones and Xiao, 2005; Al-Helal et al., 2012; Gabellone et al., 2014; Gabellone and Whitaker, 2016; Newport et al., 2017). (Fig. 11). However, the study area was located offshore and therefore seawater was likely to be of normal salinity. Nevertheless, it is possible that the topography provided by the underlying salt dome led to very shallow water conditions that could have facilitated reflux of mesohaline brines on the platform top, and possibly geothermal convection on the margins of the diapir and along fractures. It has been proposed from trace element data that fluids were sub-oxic or reducing and that there is evidence of fluid-rock interaction with underlying siliciclastic sediments. In this case, seawater that was refluxed and convected on the Amsittene Anticline could have been enriched in Mg, as well as Fe and Al, as a result of fluid-rock interaction with the underlying clastic sediments. Triassic evaporites that are interbedded within

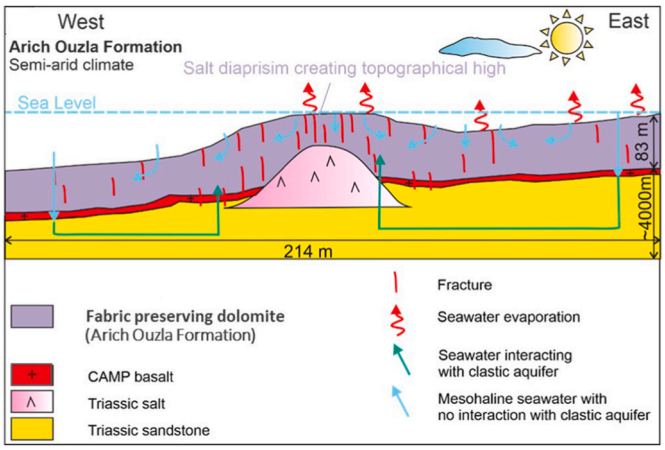

Fig. 11. Conceptual model showing dolomitization of the Arich Ouzla Formation by seawater in the Essaouira-Agadir Basin. Under semi-arid conditions during the Sinemurian, mesohaline seawater seeped through the Arich Ouzla Formation limestones by density driven flux where the limestones were replaced by FP dolomites. Due to the brittle nature of the dolomites making them subtler to fracturing, open fractures were developed as a result of Triassic salt diapirism. The open fractures were used as migration pathways for seawater convection passing through the Triassic clastic aquifer, Triassic salt and migrating up warm fluids, partially recrystallizing the FP dolomite to FD dolomite. Vertical thickness of the Arich Ouzla Formation is exaggerated in the sketch.

Triassic sandstones (Fig. 2 A) comprise halite and gypsum. Therefore, they are not likely to have contributed Mg, but could have provided an additional source of saline water during halokinesis. The localised formation of the dolomite, along with a decrease in Mg/Ca ratios towards the dolomite-limestone boundary on the margins of the body (Koeshidayatullah et al., 2022) suggests that dolomitization was limited to the salt diapir, with a marked reduction in dolomitizing potential over a short distance. The temperature determined from the limestone of the Arich Ouzla Formation of 69 °C (Table 2, Fig. 10) is in agreement with the maximum burial depth and temperature for the platform, estimated by Zühlke et al. (2004); Rimi (1993). Unlikle the FP dolomite which is non-stoichiometric, FD dolomite is stoichiometric which suggest significant recrystallization and stabilization from hot, evolved fluids that had a relatively invarient composition through time (e.g. Gregg and Sibley, 1984; Kaczmarek and Sibley, 2014). Correspondingly, the stoichiometry and clumped isotope data for FD dolomite indicates that it precipitated at temperatures higher than the FP dolomites (66–90 °C; Table 2) (Fig. 10), reflecting thinning of the crust. The oxygen and carbon isotopic values for the FD dolomites (Fig. 5 A) plot within the same region as Lower Jurassic dolomites elsewhere in the region (Tazekka District- NE Morocco: Auajjar and Boulègue, 2003; Tazoult salt wall- Central High Atlas: Moragas et al., 2019), which have been interpreted to form from hydrothermal formational brines derived from the Triassic siliciclastic acquifers with fluid expulsion along faults and fractures into the Lower Jurassic strata. However, dolomitization by this process is unlikey as brines are often of low volume unless the basin is overpressured (Frazer et al., 2014; Gomez-Rivas et al., 2015). There is therefore a mass balance problem in deriving sufficient water and Mg for dolomitization. It is proposed, based on the spatial distribution of the FD dolomites in proximity to faults and geochemical proxies, that ongoing convection of penecontemporaneous or latent seawater, modified by fluid-rock interaction during convection is the most viable dolomitizing process (e.g. Gomez-Rivas et al., 2015; Hollis et al., 2017; Cruset et al., 2021). Seawater is the most likely source of Mg due to its high Mg/Ca ratio; however, additional sources of Mg could have increased the potency of the dolomitizing fluid. For example, Mg could be released during seawater convection and interaction with underling Triassic sandstones (e.g. released during clay diagenesis). Although no evidence of illitization of clay minerals was identified in the dolomites, the presence of minor quartz and albite within the dolomites suggests interaction of brines with siliciclastic sediments. The Central Atlantic Magmatic Province basalts could also have supplied Mg, if an acidic fluid was available to leach Mg from olivine and pyroxene (e.g. Breislin et al., 2020). A single sample from the CAMP basalt was analysed and the results illustrate the presence of pyroxene, olivine and illite (Fig. 8) which could be possible sources of Mg responsible for formation of the FD dolomites. The CAMP basalt was also found to be composed of clinochlore, muscovite and vermiculite (Fig. 8) which suggests hydrothermal alteration. Basaltic sediments are often depleted in radiogenic Sr (e.g. Davis et al., 2003; Krabbenhöft et al., 2010; Pearce et al., 2015; Voigt et al., 2018), hence, it is unlikely to have contributed to the enriched $^{87}Sr/^{86}Sr$ values that were measured in the dolomite in this study. Also, a source of acidic fluid that is sufficiently acidic to leach the basalts is difficult to identify. Therefore, based on the previously presented data, the most likely source for Mg forming the FD dolomites is interaction of seawater with the Triassic sandstone.

5.5. *Dolomitization fluid flow pathways*

The Arich Ouzla Formation was deposited on a carbonate ramp (Duval-Arnould et al., 2021) where geothermal convection is unlikely to have occurred because there would be insufficient differentiation in water depth, compared to a steeply dipping platform margin, to drive convection (Aharon et al., 1987; Whitaker et al., 2004; Dong et al., 2020; Breislin et al., 2020). However, topographical variations on the Arich Ouzla Formation carbonate platform could have been created because of local salt diapirism (Zühlke et al., 2004; Hafid et al., 2006) during the LowerJurassic (Figs. 10 and 11). Convection might also have been facilitated by a thermal anomaly above the salt, as salt (halite, sylvite & anhydrite) has a thermal conductivity 2 to 4 times higher than other sedimentary rocks (Magri et al., 2008; Pauselli et al., 2021), thereby increasing fluid temperature in the vicinity of diapiric structures (Jensen, 1983; Canérot et al., 2005; Magri et al., 2008; Nader et al., 2012) (Fig. 11). The magnitude of the thermal anomaly would depend on the morphology, size and depth of the diapir. Furthermore, fractures may have formed due to salt diapirism which would have facilitated convection of seawater during the Sinemurian (Fig. 10) on the margin of the diapir. The presence of clasts of FP dolomite within the fracture corridors (Fig. 4D–F) suggests that dolomitization predated fracturing and that the position of the fracture corridors was controlled by the mechanical contrast between dolomite and limestone (Koeshidayatullah et al., 2022). The second phase of dolomite (FD dolomite) then formed by fluid flow along the fracture corridor leading to dolomite recrystallization, evidenced by the presence of dolomite cement and a lower porosity in the fracture corridor away from it. It is not possible from the current study to assess with confidence whether salt diapirism or the Alpine compression controlled the formation of the fracture corridors, but both would have occurred after formation of the FP dolomite, likely during the Cenozoic, prior to karstification (Fig. 10) (Fig. 11).

5.6. *Calcite cementation and karstification*

The white (and locally black pigmented) calcite cement (Fig. 4 D-E, 7 B and G) in pore spaces and fractures crosscutting the dolomite bodies is the penultimate diagenetic phase in the Arich Ouzla Formation. The occurrence of calcite in fractures suggests fluid flow during tectonic activity. The calcite cement shows a non-CL response (Fig. 7 H), which suggests formation in an oxic setting as it also has low concentrations of Fe (Table 1) (e.g. Meyers, 1974; Carpenter and Lohmann, 1989; Nader et al., 2008; Tostevin et al., 2016). The depleted $\delta^{18}O_{calcite}$ (Fig. 5 A, Table 2) suggests precipitation from an isotopically depleted fluid, typical of a meteoric water (Lohmann, 1988; Moore, 2001; Moragas et al., 2019; Cruset et al., 2018, 2021). Very low concentrations of Na (40.4–93.7 ppm, Table 1) in the calcite cement also supports a meteoric

origin (e.g. Nader et al., 2008). The minor quartz (0.5–1.0 %) and albite (0–0.1 %) co-existing with the calcite cements (Table 1) could suggest interaction of the meteoric water with overlying or basal siliciclastic sediments (Fig. 2 A). The calcite cement has high concentrations of Mg (5170–7980 ppm) and relatively lower concentrations of Al (average = 482–907 ppm) and Si (average = 97.9–161 ppm) (Table 1) that could all be consistent with fluid-rock interaction with siliciclastic deposits below or above the Arich Ouzla Formation and the precursor dolomite (Fig. 2 A). This suggests that calcite cementation occurred during uplift of the platform and exposure during the Cenozoic (Fig. 11). Koeshidayatullah et al. (2022) bracketed the formation of karstic fissures in the upper 5 m of the Amsitene Anticline to Eocene to Miocene based on their sedimentary fill, and similar, calcite cements with a meteoric signature occur in the Central High Atlas (Moragas et al., 2019). The presence of bitumen in the calcite cement indicates that hydrocarbon emplacement was coincident with calcite cementation (Fig. 4 E, 9, 10). This suggests that hydrocarbon emplacement occurred during basin inversion, but faulting led to leakage of the hydrocarbon to the surface. Furthermore, the low volume of porosity within much of the Arich Ouzla Formation, particularly in the vicinity of faults, means that there was little residual pore space for hydrocarbon emplacement by this time.

6. Conclusions

This paper offers the first detailed description and discussion of the diagenetic overprint of the Upper Sinemurian- Lower Pliensbachian, Arich Ouzla Formation shallow water carbonate platform that was established in the Essaouira-Agadir Basin.

(1) The Arich Ouzla Formation is characterised by inner to mid-ramp carbonate facies, consist of ooidal-oncoidal packstone-grainstone & peloidal-skeletal rich packstone/floatstone facies.
(2) FP dolomite bodies exhibit stratabound geometries, showing fine to medium crystalline planar crystal textures. The dolomite is non-stoichiometric, showing oxygen and carbon stable isotope values that are comparable to Lower Jurassic seawater, suggesting precipitation at low temperatures (<50 °C).
(3) The brittle nature of the FP dolomite together with salt diaprism/deformation during burial led to development of open fractures.
(4) Open fractures within the partially dolomitized Arich Ouzla Formation allowed continued convection of warm dolomitizing fluids which recrystallized FP dolomite to form FD dolomite.
(5) The FD dolomites are stoichiometric and show medium-coarse planar-s to nonplanar crystal morphology, dull CL response, depleted oxygen stable isotope signatures compared to Lower Jurassic seawater. They are interpreted to have originated from penecontemporaneous or latent seawater that reacted with the underlying Triassic sandstones, forming warm (66–90 °C) dolomitizing fluids that convected along fractures.
(6) Further uplift of the basin caused by local salt deformation and/or the Cenozoic Alpine Orogeny may have led to exposure of the Arich Ouzla Formation, erosion and karstification, proven by the presence of fracture corridors filled by clasts of limestones, FP dolomites and FD dolomites which are brecciated by meteoric calcites and karst fissures.
(7) Although the FP dolomites have higher porosity than the precursor limestone, porosity was largely reduced by recrystallization and formation of FD dolomite around fracture corridors.
(8) Hydrocarbon emplacement post-dated dolomitization and appears to be broadly contemporaneous with uplift, fracturing and the ingress of meteoric fluids. The presence of bitumen implies hydrocarbon degradation, probably associated with water washing during platform emergence and karstification.

CRediT authorship contribution statement

Nawwar Al-Sinawi: Data curation, Formal analysis, Methodology, Writing – original draft. **Cathy Hollis:** Conceptualization, Project administration, Supervision, Writing – review & editing. **Aude Duval-Arnould:** Conceptualization, Formal analysis. **Ardiansyah Koeshidayatullah:** Writing – review & editing. **Stefan Schröder:** Conceptualization, Project administration, Writing – review & editing, Supervision. **Jonathan Redfern:** Funding acquisition, Supervision, Writing – review & editing.

Declaration of competing interest

The authors declare that they have no known competing financial interests or personal relationships that could have appeared to influence the work reported in this paper.

Data availability

Data will be made available on request.

Acknowledgements

The first author would like to send her sincere gratitude to Petroleum Development Oman (PDO) for sponsoring her PhD studies which this manuscript is part of. We thank our colleagues/technicians at the University of Manchester for the laboratory analyses support and Dr Stephen Crowley (University of Liverpool) for stable isotope analysis. The authors appreciate Luc Bulot's work on the biostratigraphy done in a previous study within the same area which supported the age assignment of the studied formation. The appreciation is extended to the North Africa Research Group (NARG) sponsors for their considerable support to complete this study (e.g. fieldwork, conferences, meetings/discussions) and Office Nationale des Hydrocarbures et des Mines (ONHYM) for logistical support in the field. David Cruset and Jay Gregg are thanked for their detailed and helpful reviews on an earlier version of this manuscript. Mohamed Abdelsalam is thanked for his editorial support.

Appendix A. Supplementary data

Supplementary data to this article can be found online at https://doi.org/10.1016/j.jafrearsci.2023.105167.

References

Abanda, P.A., Hannigan, R.E., 2006. Effect of diagenesis on trace element partitioning in shales. Chem. Geol. 230 (1–2), 42–59.
Adams, A.E., 1979. Sedimentary environments and palaeogeography of the Western High Atlas, Morocco, during the middle and late Jurassic. Palaeogeogr. Palaeoclimatol. Palaeoecol. 28, 185–196.
Adams, A.E., Ager, D.V., Harding, A.G., 1980. Géologie de la région d'Imouzzer des Ida-ou-Tanane (Haut-Atlas Occidental). Notes et Mémoires du Service géologique du Maroc, Rabat 41 (285), 59–80.
Adams, J.E., Rhodes, M.L., 1960. Dolomitization by seepage refluxion. AAPG (Am. Assoc. Pet. Geol.) Bull. 44, 1912–1920.
Ager, D.V., 1974. Storm deposits in the Jurassic of the Moroccan High Atlas. Palaeogeogr. Palaeoclimatol. Palaeoecol. 15, 83–93.
Aharon, P., Socki, R.A., Chan, L., 1987. Dolomitization of atolls by sea water convection flow: test of a hypothesis at Niue, South Pacific. J. Geol. 95 (2), 187–203.
Al-Aasm, I.S., Crowe, R., Tortola, M., 2021. Dolomitization of Paleozoic successions, Huron Domain of southern Ontario, Canada: fluid flow and dolomite evolution. Water 13, 2449. https://doi.org/10.3390/w13172449.
Al-Helal, A.B., Whitaker, F.F., Xiao, Y., 2012. Reactive transport modeling of brine reflux: dolomitization, anhydrite precipitation, and porosity evolution. J. Sediment. Res. 82, 196–215.
Alsharhan, A.S., Sadd, J.L., 2000. Stylolites in lower Cretaceous carbonate reservoirs, U. A.E. In: Alsharhan, A.S., Scott, R.W. (Eds.), Middle East Models of Jurassic/Cretaceous Carbonate Systems, vol. 69. SEPM Special Publication, pp. 185–208.
Al-Sinawi, N.K., 2022. Dolomitization of Jurassic Carbonates in the Western High Atlas of Morocco: Processes and Implications for Reservoir Properties. PhD Thesis. The University of Manchester, p. 318.

Ambroggi, R., 1963. Etude géologique du versant méridional du Haut Atlas Occidental et de la plaine de Souss. Notes et Mémoires du Service géologique du Maroc, Rabat 157, 1–321.
Amel, H., Jafarian, A., Husinec, A., Koeshidayatullah, A., Swennen, R., 2015. Microfacies, depositional environment and diagenetic evolution controls on the reservoir quality of the Permian Upper Dalan Formation, Kish gas field, Zagros Basin. Mar. Petrol. Geol. 67, 57–71.
Auajjar, J., Boulègue, J., 2003. Dolomitization patterns of the Liassic platform of the Tazekka Pb-Zn district, Taza, eastern Morocco: petrographic and geochemical study. J. S. Am. Earth Sci. 16, 167–178.
Bahnan, A.E., Pironon, J., Carpentier, C., Barré, G., Gaucher, E.C., 2021. The diagenetic history of the giant Lacq gas field, witness to the Apto-Albian rifting and the Pyrenean Orogeny, revealed by fluid and basin modeling. Mar. Petrol. Geol. 133, 105250 https://doi.org/10.1016/j.marpetgeo.2021.105250.
Balcaen, L., De Schrijver, I., Moens, L., Vanhaecke, F., 2005. Determination of the 87Sr/86Sr isotope ratio in USGS silicate reference materials by multi-collector ICP–mass spectrometry. Int. J. Mass Spectrom. 242, 251–255.
Banner, J.L., Hanson, G., Meyers, W., 1988. Rare earth element and Nd isotopic variations in regionally extensive dolomites from the Burlington-Keokuk Formation (Mississippian); implications for REE mobility during carbonate diagenesis. J. Sediment. Res. 58, 415–432.
Banner, J.L., Hanson, G.N., 1990. Calculation of simultaneous isotopic and trace element variations during water-rock interaction with applications to carbonate diagenesis. Geochem. Cosmochim. Acta 54 (11), 3123–3137.
Bau, M., Dulski, P., 1996. Distribution of yttrium and rare-earth elements in the Penge and Kuruman iron-formations, Transvaal Supergroup, South Africa. Precambrian Res. 79, 37–55.
Beauchamp, J., 1988. Triassic sedimentation and rifting in the High Atlas (Morocco). In: Manspeizer, W. (Ed.), Triassic-Jurassic Rifting: Continental Breakup and the Origin of the Atlantic Ocean and Passive Margins. Developments in Geotectonics, vol. 22. Elsevier, New York, pp. 477–497.
Boggs, S., 2009. Petrology of Sedimentary Rocks, second ed. Cambridge University Press, New York, p. 600.
Bouaouda, M., 2007. Lithostratigraphie, Biostratigraphie, et Micropaléontologie des formations du Lias au Kimméridgien du Basin Atlantique Marocain d'El Jadida - agadir. Travaux de l'Institut Scientifique, Rabat, série géologie et géographie physique 22, 235.
Braithwaite, C.J.R., Heath, R.A., 1996. Regional geometry, petrographic variations, and origins of Upper Ordovician dolomites in Hadeland, Norway. Nor. Geol. Tidsskr. 76, 63–74.
Breislin, C., Crowley, S., Banks, V.J., Marshall, J.D., Millar, I.L., Riding, J.B., Hollis, C., 2020. Controls on dolomitization in extentional basins: an example from the Derbyshire platform, U.K. J. Sediment. Res. 90, 1156–1174.
Breislin, C., Banks, V., Crowley, S., Marshall, J.D., Millar, I., Riding, J.D., Hollis, C., 2023. Mechanisms Controlling the Localisation of Fault-Controlled Hydrothermal Dolomitization. Derbyshire Platform, UK. https://doi.org/10.1002/dep2.214. Depositional Record.
Brown, R.H., 1980. Triassic rocks of Argana Valley, southern Morocco, and their regional structural implications. AAPG (Am. Assoc. Pet. Geol.) Bull. 64, 988–1003.
Cathelineau, M., Boiron, M.C., Jakomulski, H., 2021. Triassic evaporites: a vast reservoir of brines mobilised successively during rifting and thrusting in the Oyrenees. J. Geol. Soc. https://doi.org/10.1144/jgs2020-259 jgs2020v-2259.
Canérot, J., Hudec, M.R., Rockenbauch, K., 2005. Mesozoic diapirism in the Pyrenean orogeny: salt tectonics on a transform plate boundary. AAPG (Am. Assoc. Pet. Geol.) Bull. 89, 211–229.
Cantrell, D., Swart, P., Hagerty, R., 2004. Genesis and characterization of dolomite, Arab-D reservoir, Ghawar field, Saudi Arabia. GeoArabia 9, 11–36.
Carmichael, S.K., Ferry, J.M., McDonough, W.F., 2008. Formation of replacement dolomite in the Latemar carbonate buildup, Dolomites, northern Italy: Part 1. Field relations, mineralogy, and geochemistry. Am. J. Sci. 308 (7), 851–884.
Carpenter, S.J., Lohmann, K.C., 1989. Delta ^{18} O and delta ^{13} C variations in Late Devonian marine cements from the Golden Spike and Nevis reefs, Alberta, Canada. J. Sediment. Res. 59, 792–814.
Cruset, D., Cantarero, I., Vergés, J., John, C.M., Muñoz-López, D., Travé, A., 2018. Changes in fluid regime in syn-orogenic sediments during the growth of the south Pyrenean fold and thrust belt. Global Planet. Change 171, 207–224. https://doi.org/10.1016/j.gloplacha.2017.11.001.
Cruset, D., Vergés, J., Benedicto, A., Gomez-Rivas, E., Cantarero, I., John, C.M., Travé, A., 2021. Multiple fluid flow events from salt-related rifting to basin inversion (Upper Pedraforca thrust sheet, SE Pyrenees). Basin Res. 33 (6), 3102–3136. https://doi.org/10.1111/bre.12596.
Cruset, D., Vergés, J., Muñoz-López, D., Moragas, M., Cantarero, I., Travé, A., 2023. Fluid evolution from extension to compression in the Pyrenean fold belt and Basque-Cantabrian Basin: a review. Earth Sci. Rev. 243, 104494.
Davis, A.C., Bickle, M.J., Teagle, D.A.H., 2003. Imbalance in the oceanic strontium budget. Earth Planet Sci. Lett. 211, 173–187.
Dickson, J.A.D., 1966. Carbonate identification and genesis as revealed by staining. J. Sediment. Res. 36, 491–505.
Dong, Y., Chen, H., Wang, J., Hou, M., Xu, S., Zhu, P., Zhang, C., Cui, Y., 2020. Thermal convection dolomitization induced by the Emeishan large igneous province. Mar. Petrol. Geol. 116, 104308.
Drivet, E., Mountjoy, E.W., 1997. Dolomitization of the Leduc Formation (Upper Devonian), Southern Rimbey-Meadowbrook Reef Trend, Alberta. J. Sediment. Res. 67, 411–423.
Du Dresnay, R., 1988. Répartition des dépôts carbonatés du Lias inférieur et moyen le long de la côte atlantique du Maroc: conséquences sur la paléogéographie de l'Atlantique naissant. J. Afr. Earth Sci. 7, 385–396.
Duffaud, F., 1960. Contribution à l'étude stratigraphique du bassin secondaire du Haut-Atlas Occidental (Sud-Ouest marocain). Bull. Soc. Geol. Fr. 2, 728–743.
Duffaud, F., Brun, L., Plauchut, B., 1966. Le bassin du Sud-Ouest marocain. In: Reyre, D. (Ed.), Bassins sédimentaires du littoral africain, Symposium New Delhi, vol. 1. Publication de l'Association des Services géologiques africains, Paris, pp. 5–26.
Dunnington, H.V., 1967. Aspects of diagenesis and shape change in stylolitic limestone reservoirs: 7th world petroleum congress, 2–9 April 1967. Mexico City, Mexico 2 (12129), 339–352.
Duval-Arnould, A., 2019. Controls on Stratigraphic Development of Shelf Margin Carbonates: Jurassic Atlantic Margin – Essaouira-Agadir Basin, Western Morocco. PhD Thesis. The University of Manchester, p. 307.
Duval-Arnould, A., Schröder, S., Charton, R., Joussiaume, R., Razin, P., Redfern, J., 2021. Early post-rift depositional systems of the Central Atlantic: Lower and Middle Jurassic of the Essaouira-Agadir Basin, Morocco. J. Afr. Earth Sci. 178, 104164.
Ellero, A., Ottria, G., Malusà, M.G., Ouanaimi, H., 2012. Structural geological analysis of the High Atlas (Morocco): evidences of a transpressional fold-thrust belt. Tectonics-Recent Advances 229–258.
Ellouz, N., Patriat, M., Gaulier, J.M., Bouatmani, R., Sabounji, S., 2003. From rifting to Alpine inversion: Mesozoic and Cenozoic subsidence history of some Moroccan basins. Sediment. Geol. 156, 185–212.
Frazer, M., Whitaker, F., Hollis, C., 2014. Fluid expulsion from overpressured basins: implications for Pb-Zn mineralisation and dolomitization of the East Midlands Platform, Northern England. Mar. Petrol. Geol. 55, 68–86.
Frizon de Lamotte, D., Zizi, M., Missenard, Y., Hafid, M., El Azzouzi, M., Maury, R.C., Charrière, A., Tak, Z., Benammi, M., Michard, A., 2008. The atlas system. In: Michard, A., Saddiqi, O., Chalouan, A., Frizon de Lamotte, D. (Eds.), Continental Evolution: the Geology of Morocco. Springer-Verlag, Heidelberg, pp. 133–202.
Gabellone, T., Whitaker, F., 2016. Secular variations in seawater chemistry controlling dolomitization in shallow reflux systems: insights from reactive transport modelling. Sedimentology 63, 1233–1259.
Gabellone, T., Iannace, A., Gasparrini, M., 2014. Multiple dolomitization episodes in deep-water limestones of the Triassic Lagonegro basin (southern Italy): from early reflux to tectonically driven fluid flow. J. Sediment. Res. 84, 435–456.
Gomez-Rivas, E., Martín-Martín, J.D., Bons, P.D., Koehn, D., 2015. Can stylolite networks control the geometry of hydrothermal alterations. Geotect. Res. 97, 34–36.
Gregg, J.M., Sibley, D.F., 1984. Epigenetic dolomitization and the origin of xenotopic dolomite texture. J. Sediment. Res. 54, 908–931.
Hafid, M., 2000. Triassic–early Liassic extensional systems and their Tertiary inversion, Essaouira Basin (Morocco). Mar. Petrol. Geol. 17, 409–429.
Hafid, M., Zizi, M., Bally, A., Ait Salem, A., 2006. Structural styles of the western onshore and offshore termination of the High Atlas, Morocco. Comptes Rendus 338, 50–64.
Hiatt, E.E., Pufahl, P.K., 2014. Cathodoluminescence petrography of carbonate rocks: a review of applications for understanding diagenesis, reservoir quality, and pore system evolution. Mineralogical Association of Canada Short Course 45, 75–96.
Hofmann, A., Tourani, A., Gaupp, R., 2000. Cyclicity of Triassic to Lower Jurassic continental red beds of the Argana Valley, Morocco: implications for palaeoclimate and basin evolution. Palaeogeogr. Palaeoclimatol. Palaeoecol. 161, 229–266.
Hollis, C., Bastesen, E., Boyce, A., Corlett, H., Gawthorpe, R., Hirani, J., Rotevatn, A., Whitaker, F., 2017. Fault-controlled dolomitization in a rift basin. Geology 45, 219–222.
Horita, J., 2014. Oxygen and carbon isotope fractionation in the system dolomite–water–CO2 to elevated temperatures. Geochem. Cosmochim. Acta 129, 111–124.
Jensen, P.K., 1983. Calculations on the thermal conditions around a salt diapir. Geophys. Prospect. 31, 481–489.
Jones, G.D., Xiao, Y., 2005. Dolomitization, anhydrite cementation, and porosity evolution in a reflux system: insights from reactive transport models. AAPG (Am. Assoc. Pet. Geol.) Bull. 89, 577–601.
Kaczmarek, S.E., Sibley, D.F., 2014. Direct physical evidence of dolomite recrystallization. Sedimentology 61 (6), 1862–1882.
Kahle, C.F., 1965. Possible roles of clay minerals in the formation of dolomite. J. Sediment. Res. 35 (2), 448–453.
Kim, S.T., O'Neil, J.R., 1997. Equilibrium and nonequilibrium oxygen isotope effects in synthetic carbonates. Geochem. Cosmochim. Acta 61, 3461–3475.
Koeshidayatullah, A., Corlett, H., Stacey, J., Swart, P.K., Boyce, A., Robertson, H., Whitaker, F., Hollis, C., 2020. Evaluating new fault-controlled hydrothermal dolomitization models: insights from the cambrian dolomite, western Canadian sedimentary basin. Sedimentology 67, 2945–2973.
Koeshidayatullah, A., Al-Sinawi, N., Swart, P.K., Boyce, A., Redfern, J., Hollis, C., 2022. Coevolution of diagenetic fronts and fluid-fracture pathways. Sci. Rep. 12, 9278.
Krabbenhöft, A., Eisenhauer, A., Böhm, F., Vollstaedt, H., Fietzke, J., Liebetrau, V., Augustin, N., Peucker-Ehrenbrink, B., Müller, M.N., Horn, C., Hansen, B.T., Nolte, N., Wallmann, K., 2010. Constraining the marine strontium budget with natural strontium isotope fractionations (^{87}Sr/^{86}Sr*, $\delta^{88}/^{86}$Sr) of carbonates, hydrothermal solutions and river waters. Geochem. Cosmochim. Acta 74, 4097–4109.
Land, L.S., 1980. The isotopic and trace element geochemistry of dolomite: the state of the art. In: Zenger, D.H., Dunham, J.B., Ethington, R.L. (Eds.), Concepts and Models of Dolomitization, vol. 28. SEPM Special Publication, pp. 87–110.
Lécuyer, C., Reynard, B., Grandjean, P., 2004. Rare earth element evolution of Phanerozoic seawater recorded in biogenic apatites. Chem. Geol. 204 (1–2), 63–102. https://doi.org/10.1016/j.chemgeo.2003.11.003.

Le Roy, P., Piqué, A., 2001. Triassic-Liassic Western Moroccan synrift basins in relation to the Central Atlantic opening. Mar. Geol. 172, 359–381.
Lohmann, K.C., 1988. Geochemical patterns of meteoric diagenetic systems and their application to studies of paleokarst. In: James, N.P., Choquette, P.W. (Eds.), Paleokarst, 58-80. Springer, New York.
Luber, T., 2017. Integrated Analysis of Lower Cretaceous Stratigraphy and Depositional Systems: the Essaouira-Agadir Basin of Morocco. PhD Thesis. The University of Manchester.
Lumsden, D.N., 1979. Discrepancy between thin-section and X-ray estimates of dolomite in limestone. J. Sediment. Res. 49, 429–435.
Machel, H.G., 2004. Concepts and models of dolomitization: a critical reappraisal. In: Braithwaite, C.J.R., Rizzi, G., Darke, G. (Eds.), The Geometry and Petrogenesis of Dolomite Hydrocarbon Reservoirs, vol. 235. Geological Society, London, Special Publications, pp. 7–63.
Machel, H.G., Burton, E.A., 1991. Factors governing cathodoluminescence in calcite and dolomite, and their implications for studies of carbonate diagenesis. In: BARKER, C. E., KOPP, O.C. (Eds.), Luminesnce Microscopy and Spectroscopy: Qualitative and Quantitative Applications: SEPM Short Course, vol. 25, pp. 37–58.
Mader, N.K., Redfern, J., 2011. A sedimentological model for the continental Upper Triassic Tadrart Ouadou Sandstone Member: recording an interplay of climate and tectonics (Argana Valley; south-west Morocco). Sedimentology 85, 1247–1282.
Magri, F., Littke, R., Rodon, S., Bayer, U., Urai, J.L., 2008. Temperature fields, petroleum maturation and fluid flow in the vicinity of salt domes. In: Littke, R., Bayer, U., Gajewski, D., Nelskamp, S. (Eds.), Dynamic of Complex Intracontinental Basin: the Central European Basin System. Springer, pp. 323–344.
Marzoli, A., Bertrand, H., Knight, K.B., Cirili, S., Buratti, N., Verati, C., Nomade, S., Renne, P.R., Youbi, N., Martini, R., Allenbach, K., Neuwerth, R., Rapaille, C., Zaninetti, L., Bellieni, G., 2004. Synchrony of the Central Atlantic magmatic province and the Triassic-Jurassic boundary climatic and biotic crisis. Geology 32, 973–976.
Matthews, A., Katz, A., 1977. Oxygen isotope fractionation during the dolomitization of calcium carbonate. Geochem. Cosmochim. Acta 41, 1431–1438.
McCrea, J.M., 1950. On the isotopic chemistry of carbonates and a paleotemperature scale. J. Chem. Phys. 18, 849–857.
Mclennan, S.M., Taylor, S.R., Mcculloch, M.T., Maynard, J.B., 1990. Geochemical and Nd-Sr isotopic composition of deep-sea turbidites: crustal evolution and plate tectonic associations. Geochimica et Cosmochmica Acta 54, 2015–2050.
Melim, L.A., Scholle, P.A., 2002. Dolomitization of the Capitan Formation forereef facies (Permian, west Texas and New Mexico): seepage reflux revisited. Sedimentology 49, 1207–1227.
Meyers, W.J., 1974. Carbonate cement stratigraphy of the Lake Valley Formation (Mississippian) Sacramento Mountains, New Mexico. J. Sediment. Res. 44, 837–861.
Michard, A., Saddiqi, O., Chalouan, A., Frizon de Lamotte, D., 2008. Continental Evolution: the Geology of Morocco. Springer-Verlag, Heidelberg, p. 404.
Moore, C.H., 2001. Carbonate Reservoirs—porosity evolution and diagenesis in a sequence stratigraphic framework. Dev. Sedimentol. 55.
Morabet, A.M., Bouchta, R., Jabour, H., 1998. An overview of the petroleum systems of Morocco. In: Macgregor, D.S., Moody, R.T.J., Clark-Lowes, D.D. (Eds.), Petroleum Geology of North Africa, vol. 132. Geological Society, London, Special Publications, pp. 283–296.
Moragas, M., Baqués, V., Travé, A., Martín-Martín, J.D., Saura, E., Messager, G., Hunt, D., Vergés, J., 2019. Diagenetic evolution of lower Jurassic platform carbonates flanking the Tazoult salt wall (Central High Atlas, Morocco). Basin Res. 32, 546–566.
Motte, G., Hoareau, G., Callot, J.P., Révillon, S., Piccoli, F., Calassou, S., Gaucher, E.C., 2021. Rift and salt-related multi-phase dolomitization: example from the northwestern Pyrenees. Mar. Petrol. Geol. 126, 104932.
Murray, S.T., Arienzo, M.M., Swart, P.K., 2016. Determining the Δ47 acid fractionation in dolomites. Geochem. Cosmochim. Acta 174, 42–53.
Mustaphi, H., Medina, F., Jabour, H., Hoepffner, C., 1997. Le bassin du Souss (Zone de Faille du Tizi n'Test, Haur Atlas Occidental, Maroc): resultat d'une inversion tectonique contrôlée par une faille de détachement profonde. J. Afr. Earth Sci. 24, 153–168.
Nader, F.H., Swennen, R., Keppens, E., 2008. Calcitization/dedolomitization of Jurassic dolostones (Lebanon): results from petrographic and sequential geochemical analyses. Sedimentology 55, 1467–1485.
Nader, F.H., López-Horgue, M.A., Shah, M.M., Dewit, J., Garcia, D., Swennen, R., Iriarte, E., Muchez, P., Caline, B., 2012. The Ranero hydrothermal dolomites (Albian, Karrantza Valley, northwest Spain): implications on conceptual dolomite models. Oil & Gas Science and Technology – Revue d'IFP Energies nouvelles 67, 9–29.
Nance, W.B., Taylor, S.R., 1976. Rare earth element patterns and crustal evolution-l. Australian post-Archean sedimentary rocks. Geochem. Cosmochim. Acta 40, 1539–1551.
Newport, R., Hollis, C., Bodin, S., Redfern, J., 2017. Examining the interplay of climate and low amplitude sea-level change on the distribution and volume of massive dolomitization: zebbag Formation, Cretaceous, Southern Tunisia. The Depositional Record 3, 38–59.
Newport, R., Segura, M., Redfern, J., Hollis, C., 2020. The interaction of tectonics, climate and eustasy in controlling dolomitization: a case study of Cenomanian-Turonian, shallow marine carbonates of the Iberian Basin. Sedimentology 67, 2223–2247.
Nomade, S., Knight, K.B., Beutel, E., Renne, P.R., Verati, C., Féraud, G., Marzoli, A., Youbi, N., Bertrand, H., 2007. Chronology of the central atlantic magmatic province: implications for the Central Atlantic rifting processes and the Triassic-Jurassic biotic crisis. Palaeogeogr. Palaeoclimatol. Palaeoecol. 244, 326–344.
Olanipekun, B.J., Azmy, K., 2017. In situ characterization of dolomite crystals: Evaluation of dolomitization process and its effect on zoning. Sedimentology 64, 1708–1730.
Olsen, P.E., Kent, D.V., Et-Touhami, M., Puffer, J., 2003. Cyclo-, magneto-, and bio-stratigraphic constraints on the duration of the CAMP event and its relationship to the Triassic-Jurassic boundary. In: Hames, W., McHone, J.G., Renne, P., Ruppel, C. (Eds.), The Central Atlantic Province: Insights from Fragments of Pangea, vol. 136. Geophysical Monograph, pp. 7–32.
Ouajhain, B., Daoudi, L., Laduron, D., Rocha, F., Jean, N.A.U.D., 2011. Jurassic clay mineral sedimentation control factors in the Essaouira basin (western high atlas, Morocco). Geol. Belg. 14, 129–142.
Özyurt, M., Kırmacı, Z., Al-Aasm, I.S., 2019. Geochemical characteristics of Upper Jurassic – lower Cretaceous platform carbonates in Hazine Mağara, Gümüşhane (northeast Turkey): implications for dolomitization and recrystallization. Can. J. Earth Sci. 56, 305–320.
Pauselli, C., Gola, G., Ranalli, G., Mancinelli, P., Trippetta, F., Ballirano, P., Verdoya, M., 2021. Thermal conductivity of Triassic evaporites. Geophys. J. Int. 227 (3), 1715–1729. https://doi.org/10.1093/gji/ggab293.
Pearce, C.R., Parkinson, I.J., Gaillardet, J., Charlier, B.L.A., Mokadem, F., Burton, K.W., 2015. Reassessing the stable ($\delta^{88}/^{86}Sr$) and radiogenic ($^{87}Sr/^{86}Sr$) strontium isotopic composition of marine inputs. Geochem. Cosmochim. Acta 157, 125–146.
Peybernès, B., Bouaouda, M.S., Alméras, Y., Ruget, C., Cugny, P., 1987. Stratigraphie du Lias et du Dogger du bassin côtier d'Essaouira (Maroc) avant et pendant le début de l'expansion océanique dans l'Atlantique central. Comparaison avec le bassin d'Agadir, vol. 305. Comptes-Rendus de l'Académie des Sciences, Paris, pp. 1449–1455.
Pichel, L.M., Huuse, M., Redfern, J., Finch, E., 2019. The influence of base-salt relief, rift topography and regional events on salt tectonics offshore Morocco. Mar. Petrol. Geol. 103, 87–113.
Pin, C., Briot, D., Bassin, C., Poitrasson, F., 1994. Concomitant separation of strontium and samarium-neodymium for isotopic analysis in silicate samples, based on specific extraction chromatography. Anal. Chim. Acta 298, 209–217.
Piqué, À., Le Roy, P., Amrhar, M., 1998. Transtensive synsedimentary tectonics associated with ocean opening: the Essaouira–Agadir segment of the Moroccan Atlantic margin. J. Geol. Soc. 155, 913–928. London.
Piqué, A., Tricart, P., Guiraud, R., Laville, E., Bouaziz, S., Amrhar, M., Ouali, R.A., 2002. The Mesozoic-Cenozoic atlas belt (North Africa): an overview. Geodin. Acta 15, 185–202.
Prokoph, A., Shields, G.A., Veizer, J., 2008. Compilation and time-series analysis of a marine carbonate $\delta^{18}O$, $\delta^{13}C$, $^{87}Sr/^{86}Sr$ and $\delta^{34}S$ database through Earth history. Earth Sci. Rev. 87, 113–133.
Qing, H., Bosence, D., Rose, E., 2001. Dolomitization by penesaline sea water in early Jurassic peritidal platform carbonates, Gibraltar, western Mediterranean. Sedimentology 48, 153–163.
Railsback, L., Hood, E., 2001. A survey of multi-stage diagenesis and dolomitization of Jurassic limestones along a regional shelf-to-basin transect in the Ziz Valley, Central High Atlas Mountains, Morocco. Sediment. Geol. 139 (3–4), 285–317.
Rimi, A., 1993. Geothermics of the Essaouira basin in Morocco. Can. J. Earth Sci. 30, 1049–1055.
Roch, E., 1930. Étude géologique dans la région méridionale du Maroc Occidental. Notes et Mémoires du Service géologique du Maroc, Rabat 9, 1–542.
Schettino, A., Turco, E., 2011. Tectonic history of the western Tethys since the late Triassic. Geol. Soc. Am. Bull. 123, 89–105.
Sharma, T., Clayton, R.N., 1965. Measurement of $O^{18}O^{16}$ ratios of total oxygen of carbonates. Geochem. Cosmochim. Acta 29, 1347–1353.
Sibley, D.F., Gregg, J.M., 1987. Classification of dolomite rock textures. J. Sediment. Petrol. 57, 967–975.
Simms, M., 1984. Dolomitization by groundwater-flow system in carbonate platforms. Trans. Gulf Coast Assoc. Geol. Soc. 24, 411–420.
Staudigel, P.T., Murray, S., Dunham, D.P., Frank, T.D., Fielding, C.R., Swart, P.K., 2018. Cryogenic brines as diagenetic fluids: reconstructing the diagenetic history of the Victoria Land Basin using clumped isotopes. Geochem. Cosmochim. Acta 224, 154–170.
Swart, P.K., Cantrell, D.L., Arienzo, M.M., Murray, S.T., 2016. Evidence for high temperature and 18O-enriched fluids in the Arab-D of the Ghawar field, Saudi Arabia. Sedimentology 63, 1739–1752.
Tari, G., Jabour, H., 2013. Salt tectonics along the Atlantic margin of Morocco. In: Mohriak, W.U., Danforth, A., Post, P.J., Brown, D.E., Tari, G.C., Nemcok, M., Sinha, S.T. (Eds.), Conjugate Divergent Margins, vol. 369. Geological Society, London, Special Publications, pp. 337–353.
Tostevin, R., Shields, G.A., Tarbuck, G.M., He, T., Clarkson, M.O., Wood, R.A., 2016. Effective use of cerium anomalies as a redox proxy in carbonate-dominated marine settings. Chem. Geol. 438, 146–162.
Tourani, A., Benaouiss, N., Gand, G., Bourquin, S., Jalil, N.E., Broutin, J., Battail, B., Germain, D., Khaldoune, F., Sebban, S., Steyer, J.S., 2010. Evidence of an early Triassic age (Olenekian) in Argana basin (High Atlas, Morocco) based on new chirotherioid traces. Comptes Rendus Palevol 9, 201–208.
Tourani, A., Lund, J.J., Benaouiss, N., Gaupp, R., 2000. Stratigraphy of Triassic syn-rift deposition in western Morocco. Zentralblatt für Geologie und Paläontologie 1, 1193–1215.
Veizer, J., Prokoph, A., 2015. Temperatures and oxygen isotopic composition of Phanerozoic oceans. Earth Sci. Rev. 146, 92–104.
Veizer, J., Ala, D., Azmy, K., Bruckschen, P., Buhl, D., Bruhn, F., Carden, G.A.F., Diener, A., Ebneth, S., Godderis, Y., Jasper, T., Korte, C., Pawellek, F., Podlaha, O.G., Strauss, H., 1999. $^{87}Sr/^{86}Sr$, $\delta^{13}C$ and $\delta^{18}O$ evolution of Phanerozoic seawater. Chem. Geol. 161, 59–88.

Vergés, J., Moragas, M., Martín-Martín, J.D., Saura, E., Casciello, E., Razin, P., Grelaud, C., Malaval, M., Joussiame, R., Messager, G., Sharp, I., Hunt, D.W., 2017. Salt tectonics in the atlas moutains of Morocco. In: Soto, J.i., Flinch, F.F., Tari, G. (Eds.), Permo-Triassic Salt Provinces of Europe, North Africa and the Atlantic Margins, pp. 563–579.

Videtich, P.E., 1981. A method for analyzing dolomite for stable isotopic composition. J. Sediment. Res. 51, 661–662.

Voigt, M., Pearce, C.R., Baldermann, A., Oelkers, E.H., 2018. Stable and radiogenic strontium isotope fractionation during hydrothermal seawater-basalt interaction. Geochem. Cosmochim. Acta 240, 131–151.

Warren, J.K., 2000. Dolomite: occurrence, evolution and economically important associations. Earth Sci. Rev. 52, 1–81.

Whitaker, F.F., Xiao, Y., 2010. Reactive Transport Modelling of early burial dolomitization of carbonate platforms by geothermal convection. AAPG (Am. Assoc. Pet. Geol.) Bull. 94, 889–917.

Whitaker, F.F., Smart, P.L., Jones, G.D., 2004. Dolomitization: from conceptual to numerical models. Geological Society, London, Special Publications 235 (1), 99–139.

Whiteside, J.H., Olsen, P.E., Kent, D.V., Fowell, S.J., Et-touhami, M., 2007. Synchrony between the Central Atlantic magmatic province and the Triassic-Jurassic mass-extinction event? Palaeogeogr. Palaeoclimatol. Palaeoecol. 244, 345–367.

Wierzbicki, R., Dravis, J.J., Al-Aasm, I., Harland, N., 2006. Burial dolomitization and dissolution of Upper Jurassic Abenaki platform carbonates, deep Panuke reservoir, Nova Scotia, Canada. AAPG (Am. Assoc. Pet. Geol.) Bull. 90, 1843–1861.

Zühlke, R., Bouaouda, M.-S., Ouajhain, B., Bechstädt, T., Leinfelder, R., 2004. Quantitative Meso-Cenozoic development of the eastern central Atlantic continental shelf, western High Atlas, Morocco. Mar. Petrol. Geol. 21, 225–276.